8-2018

Proton Doping and Characterization of Rare Earth Nickelates

Derek Karl Wittenburg Schwanz
Purdue University

PROTON DOPING AND CHARACTERIZATION OF RARE EARTH NICKELATES

by

Derek Karl Wittenburg Schwanz

A Dissertation

Submitted to the Faculty of Purdue University

In Partial Fulfillment of the Requirements for the degree of

Doctor of Philosophy

School of Materials Engineering

West Lafayette, Indiana

August 2018

THE PURDUE UNIVERSITY GRADUATE SCHOOL
STATEMENT OF COMMITTEE APPROVAL

Dr. Shriram Ramanathan, Chair
School of Materials Engineering
Dr. David F. Bahr
School of Materials Engineering
Dr. R. Edwin García
School of Materials Engineering
Dr. Elliott B. Slamovich
School of Materials Engineering

Approved by:
Dr. David F. Bahr
Head of the Graduate Program

To my family for all their guidance, support, and love.

ACKNOWLEDGMENTS

I would like to sincerely thank my Ph. D. advisor Shriram Ramanathan for his support, guidance, and patience over the course of this project. I cannot express how grateful I am for the opportunity to research with you and push the boundaries of human knowledge. I would also like to acknowledge my committee of Prof. David Bahr, Prof. Edwin García, and Prof. Elliott Slamovich for their advice and support throughout my graduate career.

A big thank you to the Ramanathan research group including Dr. Zhen Zhang, Dr. Fan Zuo, Dr. Koushik Ramadoss, Dr. Yifei Sun, Dr. Narayana Achari, Dr. Hai-Tian Zhang, and Chengzi Huang. It has truly been a great experience having such high level conversations with all of you, and working alongside you in the lab over the past few year, specifically Zhen.

This extent and depth of this project would not have been possible without amazing collaborators, and as such, I would like to give a special thanks to Dr. Joe Dura from NIST for his instruction regarding reflectometry data and analysis and help with data collection and experimental design. It has always been a pleasure working with you and learning new physics. I would also like to acknowledge Dr. Hua Zhou at Argonne for his advice, ideas, and time spent collecting phenomenal data together.

I would also like to thank everyone at Purdue with whom I was able to connect over the past few years including my family at University Lutheran Church, my friends in the MSE department, and others throughout campus. It has truly been a journey.

Finally, I would like to thank my family for their encouragement over the past five years. I will never forget your unconditional love and support in all my endeavors. I could not have asked for a more supportive group. Thank you Roxie, Heidi, Gretchen, Kersten, and Solomon. I love you guys.

TABLE OF CONTENTS

LIST OF TABLES vii
LIST OF FIGURES viii
ABSTRACT xi
1. INTRODUCTION 1
1.1 Perovskites 1
1.2 Rare Earth Nickelates 1
1.2.1 Phase Transition 3
1.2.2 Electron Doping and Sensing 4
1.2.3 Thin Film Growth 7
1.3 Comparison to Traditional Semiconductors 8
2. LIGHT ELEMENT DOPING OF SAMARIUM NICKELATE 10
2.1 Introduction to Light Element Doping 10
2.2 Materials and Methods 10
2.3 Property Modulation in SNO films upon doping 14
2.3.1 Absence of Externally Applied Fields 14
2.3.2 Processing Variation through the Manipulation of Doping Parameters 17
3. EFFECTS OF MODIFIED FIELD FUNCTION ON DOPING 23
3.1 Principles of Cyclic Voltammetry 23
3.2 Sweeping Voltammetry of Samarium Nickelate 25
3.2.1 Effects of Solution on Voltammetry 27
3.2.2 Scan Rate Dependence on Doping 28
4. STRUCTURAL CHANGES IN SAMARIUM NICKELATE 31
4.1 Introduction 31
4.2 X-ray and neutron scattering 31
4.3 Structural changes during potentiostatic doping 33
4.3.1 X-ray Diffraction 33
4.3.2 X-ray Reflectometry 34
4.3.3 Neutron Reflectometry 36
4.4 Structural changes during Cyclic Voltammetry 39

4.4.1 X-ray Diffraction 40
4.4.2 Neutron Reflectometry 41
4.5 Cycling Effects on Structure 43
4.6 Structure – Processing – Property Relation 44
5. VARIATION OF DOPING IN RARE EARTH NICKELATES 46
5.1 Water-Mediated phase transition of $RNiO_3$ 46
5.2 $RNiO_3$ Trends in Cyclic Voltammetry 46
5.3 Resistance Switching for $RNiO_3$ 48
6. CONCLUSIONS AND FUTURE WORK 51
6.1 Summary of RNO_3 Characterization 51
6.2 Implications of Water-Mediated Phase Transition 51
6.3 Avenues for Future Studies of $RNiO_3$ doping 53
APPENDIX. NEUTRON REFLECTOMETRY FITTING 15
REFERENCES 18

LIST OF TABLES

A.1 Variable ranges for the Neutron Simulation 16

LIST OF FIGURES

Figure 1-1 (a) Perovskite $RNiO_3$ crystal structure and (b) distortion that occurs when there is a mismatch in ionic radii [5]. 2
Figure 1-2 Cell parameters of rare earth nickelates as a function of tolerance factor *t* [7]. 3
Figure 1-3 MIT for $RNiO_3$ as a function of tolerance factor *t* [14]. 4
Figure 1-4 Molecular orbitals of SNO insulators comparing (a) charge disproportionation and (c) electron doping as well as their respective schematic band diagrams highlighting the differences in phase transitions. E_g is the band gap, *U* is the Couloumb and exchange interactions [11]. 5
Figure 1-5 Physical manifestations of electron doping in $SmNiO_3$ (a) Resistivity switching [11] and (b) Optical switching [28] 6
Figure 1-6 Necessary oxygen partial pressure and temperature to stabilize $RNiO_3$. Symbols on the charts represent experimental data from the literature [32] 7
Figure 2-1 Temperature dependent plots comparing sample quality as a function of (a) resistivity and (b) the derivative of the resistivity highlighting a metal-insulator transition..... 11
Figure 2-2 X-ray Diffraction comparing high quality and low quality SNO samples..... 12
Figure 2-3 Three-terminal cell setup used for doping and electrochemical characterization..... 13
Figure 2-4 Temperature dependent plots comparing effects of NaCl solution exposure as a function of (a) resistivity and (b) the derivative of the resistivity highlighting a metal-insulator transition. 15
Figure 2-5 Stability of SNO during acidic and basic exposure 16
Figure 2-6 (a) pH dependence of the open circuit potential (V_{OC}) for SNO films tested in different buffer solutions..... 17
Figure 2-7 Resistivity change in SNO thin films for different biases..... 18
Figure 2-8 (a) Optical modulation accompanying phase change..... 19
Figure 2-9 Resistivity vs. temperature showing reversible phase transition. 20
Figure 2-10 Non-volatility of phase transition applied over different time periods. 21
Figure 3-1 Comparison of (a, c, e) potentiostatic and (b, d, f) sweeping voltammetry and the expected relationships between the different methods. 23

Figure 3-2 Cyclic voltammograms highlighting the difference between (a) reversible reactions and (b) quasi-reversible reactions when scan rate is changed. Adapted from Bates et. al [62] 25
Figure 3-3 Cyclic Voltammogram of SNO in 10 mM NaCl. 25
Figure 3-4 Linear sweep voltammetry comparing SNO in basic and acidic solutions. 27
Figure 3-5 (a) Scan rate dependence of current vs. potential for SNO in citric acid and (b) fitting to the modified Randles-Sevcik equation. 29
Figure 4-1 Atomic cross sections for x-rays and neutrons [68]. 32
Figure 4-2 X-ray Diffraction of pristine and hydrogenated SNO for (a) wide range 2Θ and (b) synchrotron zoomed in on the SNO (220) peak 34
Figure 4-3 X-ray Reflectivity of SNO/LAO thin films highlighting the similarities with treatment using different salt solutions for (a) full Q scanand (b) normalized Q scan highlighting peak shift. 35
Figure 4-4 X-ray Reflectivity of In-situ SNO treated with subsequent bias experiments (a) full scan and (b) normalized region highlighting film peak shift 36
Figure 4-5 Neutron Reflectivity of SNO treated with H_2O and D_2O (a) full scan with simulated data fit and (b) normalized region highlighting film similar peak shift 37
Figure 4-6 Comparison of neutron scattering length density (SLD) profiles of the SNO films treated with H_2O and D_2O solutions. Profiles are simulated best fit models from the neutron data in Figure 4-4. 39
Figure 4-7 Current vs. Voltage voltammogram for SNO/LAO with marked points of interest. .. 40
Figure 4-8 XRD corresponding to points on the cyclic voltammogram highlighting the film ‘breathing’ during the hydrogenation and dehydrogenation processes. 41
Figure 4-9 (a) NR raw data and simulated fits and (b) Calculated SLD profiles for points of interest on the cyclic voltammogram of SNO 42
Figure 4-10 (a) NR raw data and simulated fits and (b) Calculated SLD profiles for multiple hydrogenation and dehydrogenation cycles. 44
Figure 4-12 Resistivity change as a function of XRD peak shift. 45
Figure 5-1 Comparison of $RNiO_3$ cyclic voltammograms 47
Figure 5-2 Comparison of maximum current density during doping as a fucntion of A-site radius. 48

Figure 5-3 Comparison of Resisistance changes for various $RNiO_3$ phase transitions for brief electrostatic pulses. 49
Figure 5-4 Trends for $RNiO_3$ resistance changes as a function of ionic radius for -2.0 V applied for (a) 0.1 s and (b) 10 s. 50
Figure 6-1 Potential electric field sensing application for $RNiO_3$ (a) resistance modulation for applied stimuli and (b) the electric field produced by various aquatic animals and vehicles that may be detected by such fields. The dotted line is extrapolation towards the limits of detectability with high precision equipment [73-78]. 53
Figure 0-1 Readouts from Refl1d fitting software (a) the SLD profile and overlay with the data. (b) sld profile and variance in comparison to the data. (c) histograms of the frequency of variables taking certain values (d) association between different parameters in the model and (e) summary of data. 17

ABSTRACT

Author: Schwanz, Derek K. W. PhD
Institution: Purdue University
Degree Received: August 2018
Title: Proton Doping and Characterization of Rare Earth Nickelates
Major Professor: Dr. Shriram Ramanathan

Perovskite rare earth nickelates with formula $RNiO_3$ (R = trivalent rare earth element) feature exceptional electrical behavior and performance in a wide variety of functional applications due to their unique metal-insulator transition. This distinctive phase transition is caused by charge disproportionation as the crystal structure distorts upon temperature change and electron-electron interactions result in a modified band structure. However, electron doping of the same nickelate systems has created a more pronounced phase transition wherein unprecedented resistivity changes on the order of 10^{10} Ω*cm are achieved through the opening of a wide bandgap. In this work, a new method for inducing a water-mediated electrically driven phase transition is examined through the use of various processing methods and investigation of subsequent effects on the structural and material properties. Electrochemically driven doping of protons is caused through potentiostatic bias applications and linear sweep voltammetry, while the effects on the electrical and optic properties are observed and correlated with structural data collected through x-ray and neutron scattering. Finally, the effects of A-site substitution (Sm, Nd, Eu) on the doping process are assessed.

1. INTRODUCTION

1.1 Perovskites

There are many unique materials that have the ABO_3 perovskite crystal structure. An ideal perovskite crystal structure occupies the cubic space group Pm-3m and has three types of ions in it: A – the larger cation, B – the smaller cation, and O – the oxygen anion [1], [2]. The B cations have a coordination of 6 with respect to oxygen anions, forming BO_6 octahedra. These octahedra form an anion corner-sharing network throughout which the A-site cations are dispersed with 12-fold coordination [3]. The perovskite lattice forms the structural basis into which many different elements may be substituted on the A and B sites, leading to a family of materials possessing a wide range of material properties [4]. In this dissertation, electrochemical doping and characterization of rare earth nickelates, a sub-family of perovskites, will be examined in great detail. Many of the results explored here can also be found in the Nature article "Perovskite nickelates as electric-field sensors in salt water" doi: 10.1038/nature25008 [5].

1.2 Rare Earth Nickelates

Perovskites having the formula $RNiO_3$ (R = trivalent rare earth lanthanide ions: La^{3+}, Nd^{3+}, Eu^{3+}, etc.) are considered rare earth nickelates where Ni^{3+} resides on the B site in the lattice, and R^{3+} resides on the A site [6]. Deviation from the ideal perovskite cubic crystal structure occurs if the ratio of the atomic radii falls outside the exact distances calculated to be

$$d_{R-O} = \sqrt{2} d_{Ni-O}$$

Where *d* is the interatomic spacing between the constituent perovskite ions. As a family of materials having a wide range of ionic radii, rare earth nickelates largely fall outside the exact distance specifications for perfect cubic crystal formation. Therefore, as the ratio between the Ni^{3+} and R^{3+} changes throughout the lanthanide series, the structure must distort in order to accommodate the mismatch. Figure 1-1 shows the perovskite structure for $RNiO_3$ as well as the distortions which stabilize the structure for ionic size mismatch. This degree of distortion can be determined by the ratio, which is defined as the tolerance factor *t* [7].

$$t = \frac{d_{R-O}}{\sqrt{2}d_{Ni-O}}$$

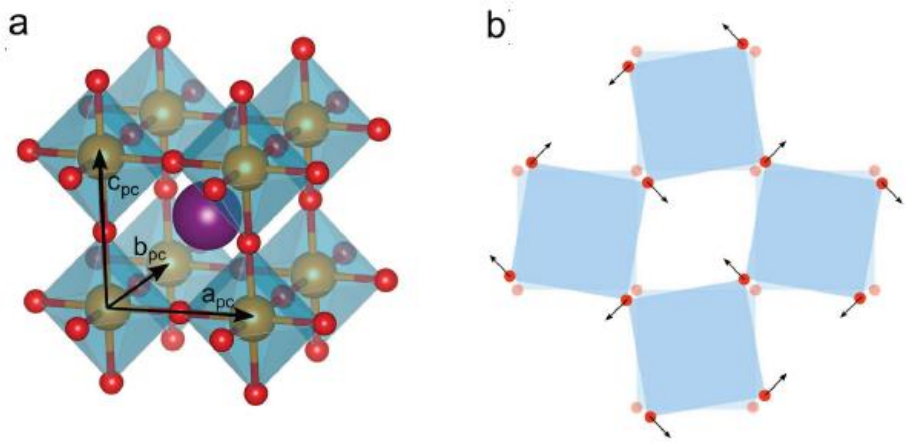

Figure 1-1 (a) Perovskite $RNiO_3$ crystal structure and (b) distortion that occurs when there is a mismatch in ionic radii adapted from [7].

The crystal symmetry each nickelate will take on depends upon *t*. Between 0.9 and 1 (ideal), the NiO_6 octahedra distort and rotate along the [110] and [001] directions to form orthorhombic *Pbnm* symmetry [7]. All rare earth nickelates aside from $LaNiO_3$ have this orthorhombic structure and symmetry. Figure 1-2 tabulates the deviation in $RNiO_3$ unit cell parameter as a function of

tolerance factor. As such, it is worth noting that as the atomic weight increase, ionic radius decreases and the $RNiO_3$ structures become less stable as the deviation from ideal perovskite increases.

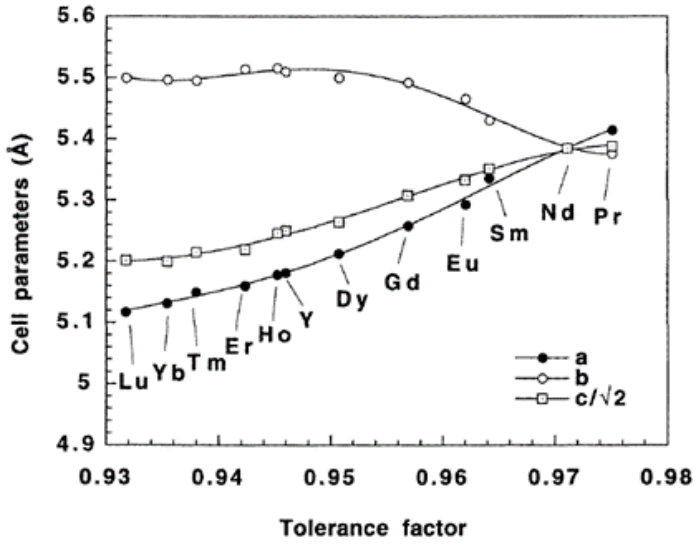

Figure 1-2 Cell parameters of rare earth nickelates as a function of tolerance factor *t* adapted from [8].

1.2.1 Phase Transition

The metal insulator transition (MIT) is a characteristic temperature at which rare earth nickelates suddenly switch behavior. Above this hallmark temperature, the nickelates act as metals, but as they are cooled below the MIT, they switch to insulating behavior. This phenomena is the manifestation of the NiO_6 octahedra buckling below the MIT temperature, resulting in *d* orbital interaction and overlap in the crystal structure [9], [10]. In a material such as $RNiO_3$, which will have Ni^{3+} in an octahedral coordination, the 5 degenerate Ni^{3+} *d* orbitals split into t_{2g} and e_g orbitals [11]. Ultimately, charge disproportionation or ordering is one proposed mechanism for this phase

transition between metallic and insulating behavior [12]. Figure 1-3 depicts the variation in the MIT temperature as it relates to the tolerance factor for the $RNiO_3$ family. It is worth reiterating here that the higher atomic weight lanthanides have greater lattice distortion, are generally less stable, and have lower MIT temperatures.

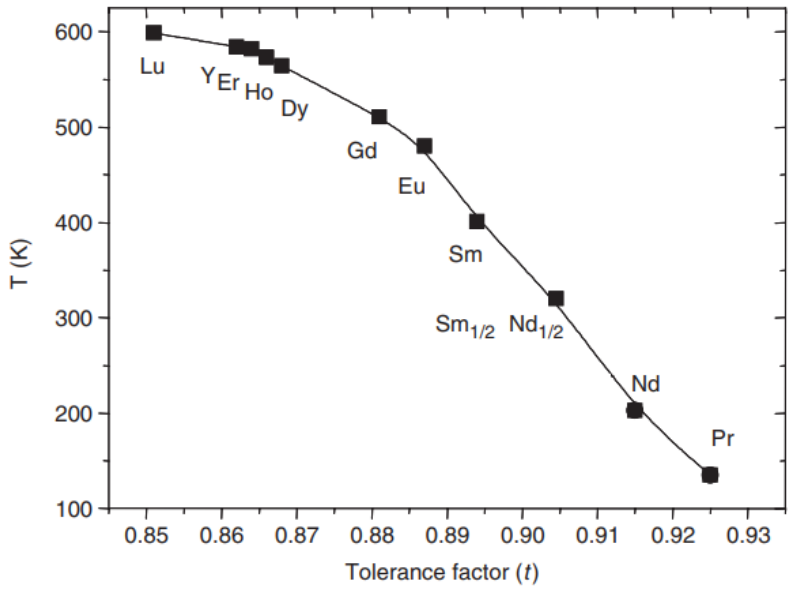

Figure 1-3 MIT for $RNiO_3$ as a function of tolerance factor *t* adapted from [6].

1.2.2 Electron Doping and Sensing

There are many device applications leveraging the unique properties of $RNiO_3$ including supercapacitors [13], [14], opto-electronic devices [11], [15], gas sensors[16], [17], solid oxide fuel cells [18], and other resistance switching devices [19]–[21]. Most of these applications utilize the characteristic MIT to achieve high performance. Recently, an alternative method for driving a phase transition through electron doping has been discovered, directly adding negative charge carriers to the e_g orbital [11], [19]. Even though the typical MIT in $RNiO_3$ materials is thermally

driven and likely caused by charge disproportionation, with electron doping, a new band gap opens as the newly added electrons experience Columbic repulsion from existing electrons in the structure [11]. Figure 1-4 shows a comparison of the band structures for the different phase transitions.

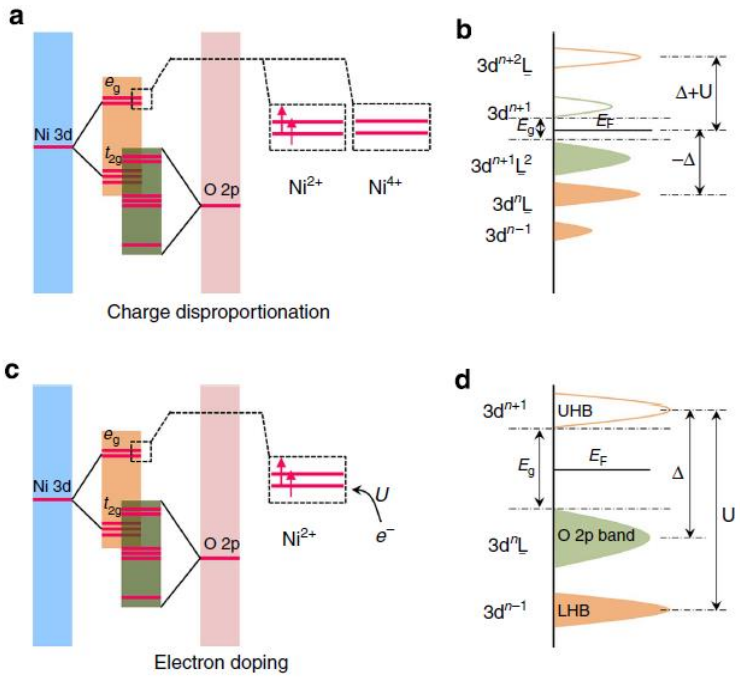

Figure 1-4 Orbitals of SNO insulators comparing (a) charge disproportionation and (c) electron doping as well as their respective schematic band diagrams highlighting the differences in phase transitions. E_g is the band gap, U is the Couloumb and exchange interactions [11].

The electron doping process causes significant changes to the properties of the oxide material. Fundamentally, these changes occur through the addition of small elements such as H^+ or Li^+, where the small metal cations will bind to the O^{2-} in the structure, freeing the electron to go into the orbitals [11], [22]. It is necesasry to use dopant elements that have lower electronegitivity than Ni so the electron will separate. Two primary ways to achieve electron doping of nickelates are annealing in H_2 gas and ionic liquid gating [11], [19]. In the annealing

process, Pt bars are patterened on the surface and as the sample is annealed in H_2 gas, the triple phase boundary between the Pt, nickelate, and gas allows for dissociation of the H_2 molecules and diffusion of H^+ into the film [11]. Contrairily, in the ionic liquid gating experiments, Li^+ is electrochemically driven into the lattice from a Li^+ salt containing solution with an applied electrical bias [19]. In both cases, there is significant modulation in the properties as this new phase transition occurs. Figure 1-5 shows resistivity switching and optical modulations that accompany this phase transition.

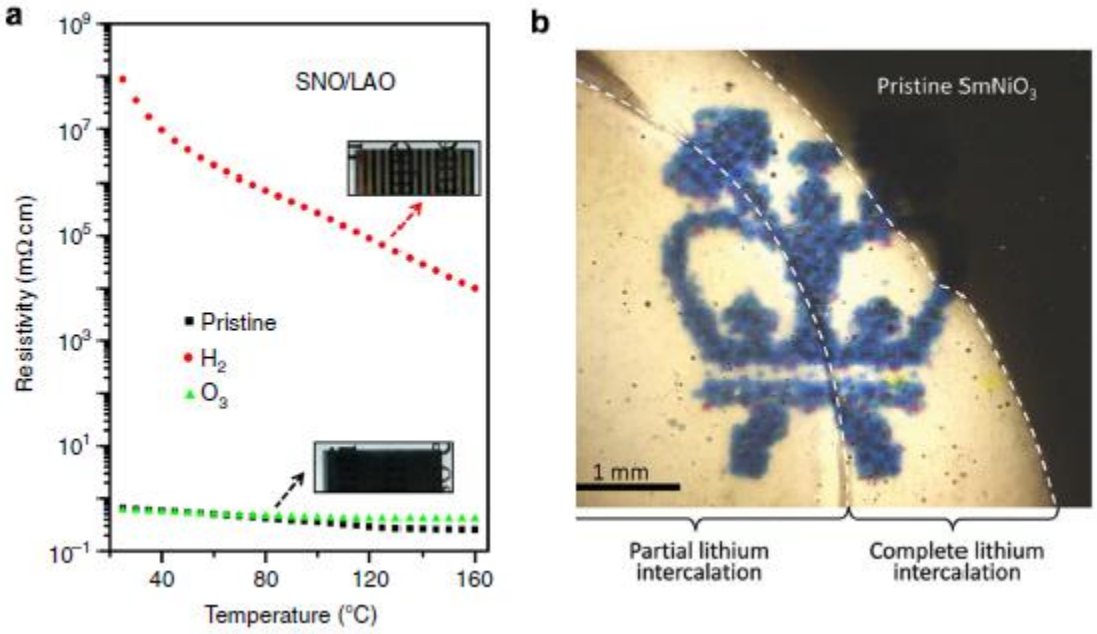

Figure 1-5 Physical manifestations of electron doping in $SmNiO_3$ (a) Resistivity switching [11] and (b) Optical switching [19].

1.2.3 Thin Film Growth

Rare earth nickelates are grown in a variety of ways depending on the intended application, with epitaxial thin films being preferable for high performance and unique [20], [23]. For bulk processing of these oxides, formation typically follows the formula

$$R_2O_3 + 2NiO + \frac{1}{2}O_2 \leftrightarrow RNiO_3$$

In this chemical equation, the presence of sufficient oxygen on the reactant side will drive the reaction towards formation of the $RNiO_3$ [24]; however, if there is insufficient oxygen during the reaction, a mixed oxide system will be more energetically favorable to the single perovskite phase.

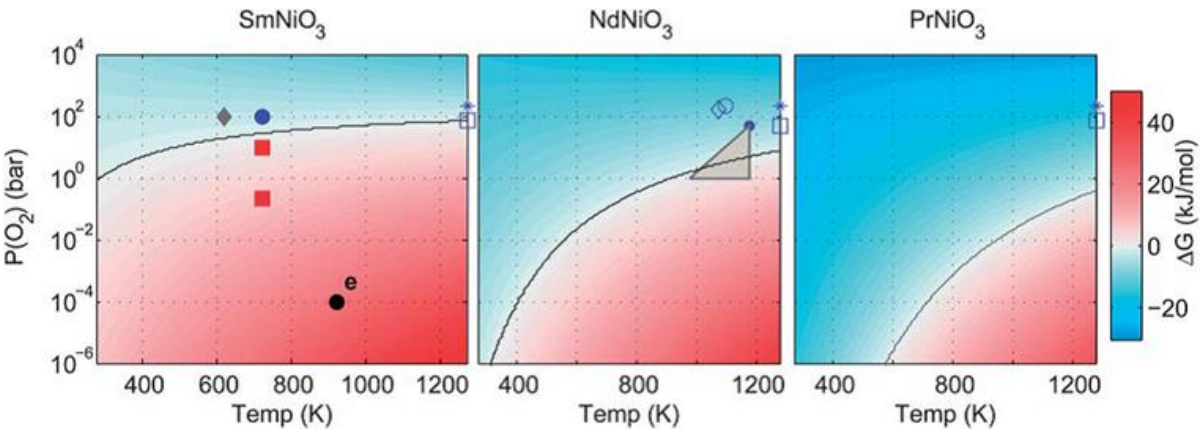

Figure 1-6 Necessary oxygen partial pressure and temperature to stabilize $RNiO_3$. Symbols on the charts represent experimental data from the literature [24].

Due to the changes in structural distortion and stability within the $RNiO_3$ family, it follows that there would be differences in the stabilization energy required to create perovskite structure. As the atomic weight and distortion both increase in the family, it becomes more difficult to stabilize the nickelates under ambient conditions. Figure 1-6 depicts the required oxygen partial

pressure to form stable nickelates. In these plots, the blue represents a negative Gibbs free energy of formation indicating that the perovskite phase will be thermodynamically stable, whereas red and white outline areas where mixed oxides are more favorable [24]. These thermodynamic calculations offer a blueprint for the necessary processing to obtain quality perovskite structures of a given composition.

As is typical of thin film oxides, $RNiO_3$ are fabricated using deposition techniques such as sol-gel, magnetron sputtering, evaporation, and pulsed laser deposition [25]–[29]. However, post-processing is usually necessary due to the instability caused by distortions in the perovskite structure. In the case of $SmNiO_3$ (SNO), Figure 1-6 predicts a metastable phase under ambient temperature and O_2 partial pressure, and as such, high pressure O_2 annealing is necessary for proper phase formation, specifically with polycrystalline films grown on substrates such as Si [24]. Phase formation can also be stabilized through the use of epitaxial strain on substrates such as $LaAlO_3$ (LAO), $SrTiO_3$ (STO), $NdGaO_3$ (NGO) and MgO [25], [26]. Strain matching with these substrates can be utilized to not only epitaxially grow the structure, but also to tune the MIT. A substrate with a closer matching lattice parameter will have the sharpest phase transition indicating this characteristic phenomena can be influenced by small changes to the crystal structure [26].

1.3 Comparison to Traditional Semiconductors

There are many materials outside the $RNiO_3$ perovskite family that have utility in a wide range of applications. Some semiconducting oxides such as ZnO, In_2O_3 and WO_3 have been utilized as gas sensors [30]–[32]. These oxides operate at elevated temperatures and demonstrate a change in electrical resistance in the presence of certain gases. [30]–[33]. Their sensing capability is attributed to the adsorption and reaction at the oxide-gas interface [34]–[36]. As a

prototypical example, WO_3 based sensors gain their functionality when oxygen vacancies are formed on the oxide surface during CO gas sensing. These vacancy formations cause charge filling into the conduction band and subsequent decrease in electrical resistance [35]. Aside from uses as gas sensors, WO_3 is also an intensively studied electrochromic material [37]–[41]. In this type of application, WO_3 changes from a transparent to optically blue and shows a decrease in electrical resistance upon the electrochemical insertion of small cations such as H^+, Li^+, Na^+ [35], [37], [38], [42]–[44]. Similar to the creation of oxygen vacancies causing the gas sensor functionality, the insertion of cations simultaneous causes charge balancing electrons to fill into the conduction band of WO_3 [35]. It has been reported that the resistance of WO_3 decreases by nearly four orders of magnitude per 1*e*/WO_3 [41], [44], [45]. This phenomena is in stark contrast to that of perovskite nickelates such as $SmNiO_3$ (SNO), wherein charge filling results in half filled e_g orbitals, and Mott-Hubbard strong electron localization appears [11], [19]. Proton intercalation into SNO enables an increase in electrical resistance up to 10 orders of magnitude per 1*e*/SNO [11], [18]. Therefore, such half-filling induced electron localization mechanisms observed in the $RNiO_3$ family would enable a resistance change greater than ~10,000x than that of WO_3 and other conventional semiconductors, thus enabling $RNiO_3$ materials to be studied for use in highly sensitive applications.

2. LIGHT ELEMENT DOPING OF SAMARIUM NICKELATE

2.1 Introduction to Light Element Doping

Although conventional means of doping semiconductors such as $SmNiO_3$ (SNO) involve electron doping and proton intercalation through a triple phase point on Pt electrodes [11], [19], this type of doping method limits the area of the doped electrodes to the geometry confined around the electrodes and would necessitate incorporation of the electrodes into the device geometry. Alternative methods to dope semiconductors using solutions have been utilized for other semiconductor systems such as WO_3 [35], [37], [40]. This chapter focuses on the SNO film preparation and successive doping utilizing aqueous media and potentiostatic bias applications to induce a water-mediated phase transition.

2.2 Materials and Methods

Physical Vapor deposition and subsequent ultrahigh pressure annealing in pure O_2 was used to fabricate SNO thin films. Substrates were cleaned with acetone, deionized water, and isopropanol followed by drying with Ar gas. SNO films were then deposited by magnetron co-sputtering of Sm and Ni targets at room temperature in Ar/O_2 mixture at 5 mTorr with power of Sm 160 W (Radio Frequency) and Ni 80 W (Direct Current) respectively. This ratio was used and adjusted as necessary throughout experiments because it made for a stoichiometric film as analyzed by energy-dispersive x-ray spectroscopy (EDS). The substrates were rotated during deposition to ensure the compositional homogeneity. The deposited samples were then annealed at 500 °C for 24 hours at high pressure of O_2 (100 bar) in a home built autoclave. Both epitaxial

and polycrystalline SNO thin films were utilized in this work to demonstrate the generality of the phenomena discussed later in this chapter. Epitaxial SNO thin films were obtained with growth on single crystalline $LaAlO_3$ (001) substrates, while polycrystalline SNO thin films were grown on Si (100) wafers.

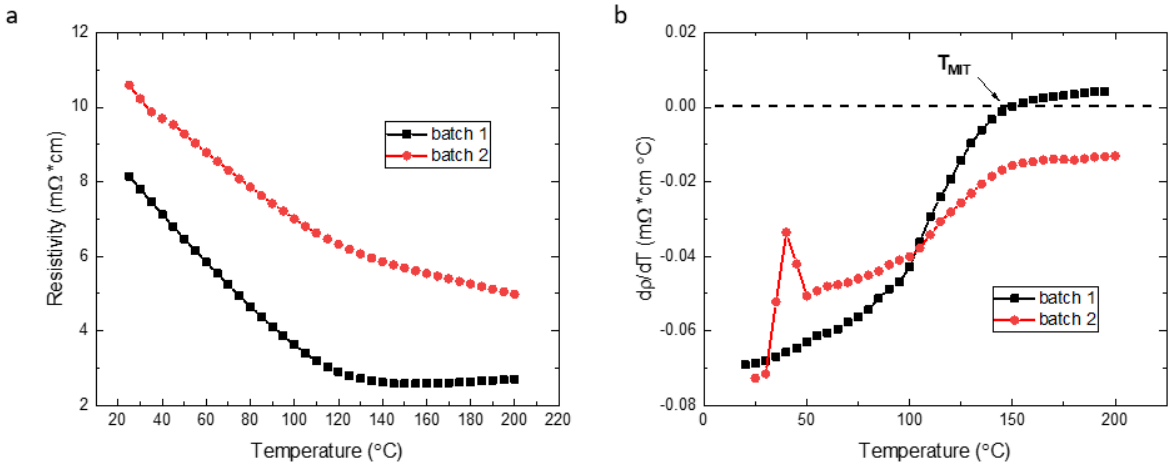

Figure 2-1 Temperature dependent plots comparing sample quality as a function of (a) resistivity and (b) the derivative of the resistivity highlighting a metal-insulator transition.

One of the challenges for achieving sufficient perovskite crystallization of the SNO is establishing sample uniformity throughout all tests with the deposition and annealing processes. However, this sometimes proved difficult due to a wide range of processing variability such as slight changes in the sample loading position, differing heat zones in the furnace, and inconsistent pressure in the autoclave due to leaks. Figure 2-1 shows the resistance vs. temperature plots and their derivatives for two different SNO/LAO samples prepared under the exact same conditions. The sample from batch 1 shows a distinct metal insulator transition (MIT) near 150 °C where the slope of the resistance vs. temperature plot changes slope. In contrast, the sample from batch 2

does not show a MIT and is likely not fully formed SNO. The second sample also has a slightly higher resistivity.

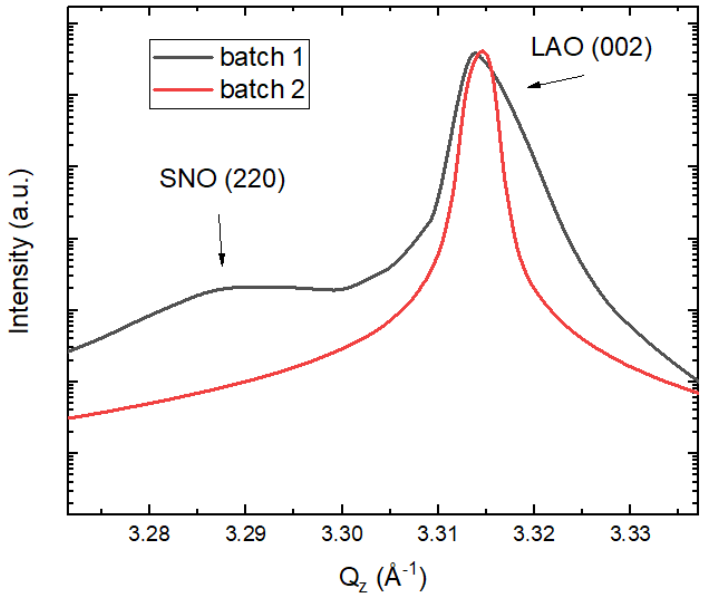

Figure 2-2 X-ray Diffraction comparing high quality and low quality SNO samples.

Figure 2-2 shows the corresponding X-ray diffraction (XRD) patterns for these two batches. From this plot, it is apparent that the sample from batch 1 shows a distinct (002) SNO peak near $2\Theta = 38.1°$. This peak does not appear for the sample from batch 2, and even though the samples were prepared in exactly the same manner, batch to batch variability caused the samples in batch 2 to be poor. For all the nickelate samples prepared in this study, the characteristic MIT was tested in order to ensure a baseline quality of the thin films compared in testing.

Proton doping of SNO thin films was performed in aqueous salt solutions using several salts and concentrations including dissolved reagent grade NaCl, KOH and citric acid in micropure

water (18.2 MΩ·cm). Experiments were performed at ambient temperatures and conditions unless otherwise noted. Additional standard buffers (pH = 4.0, 7.0, and 10.0) were used in some experiments. These different aqueous environments were designed to cover a wide range of temperature pH in order to determine different effects of solution on the doping process throughout the experiments.

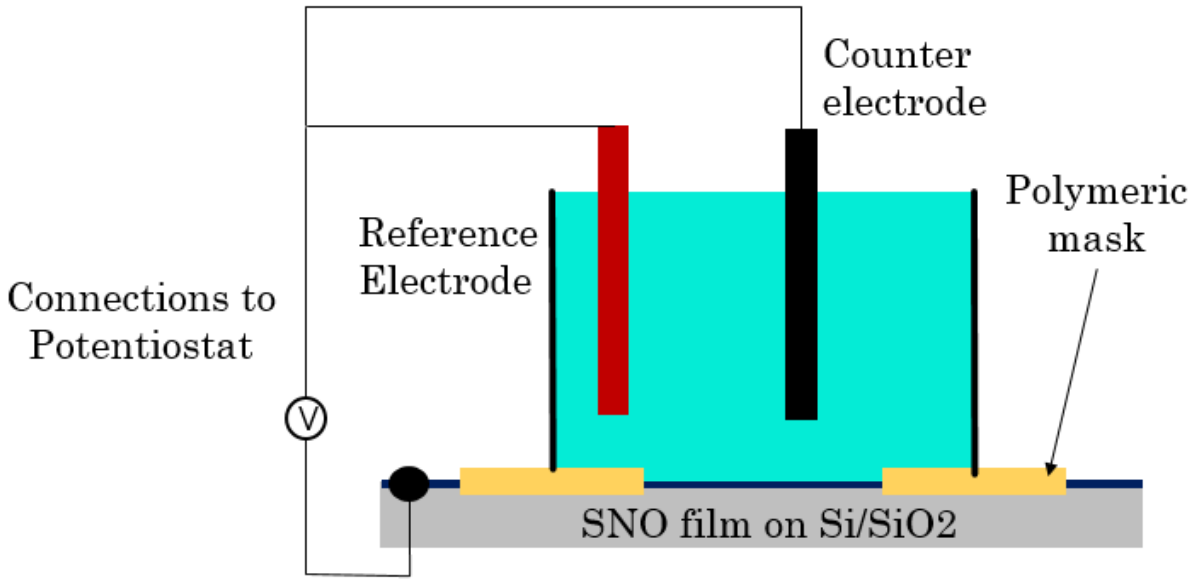

Figure 2-3 Three-terminal cell setup used for doping and electrochemical characterization.

SNO thin films were incorporated into a three-terminal cell as shown in Figure 2-3. Pt wire was bonded to the surface of SNO with silver paste. Gamry polyethylene masks were utilized to exposed selected areas of SNO to the solution for treatment. The SNO was then submerged into aqueous solution and connected as a working electrode. The counter electrode used was a graphite rod with a large surface area. It is important that the surface area of this counter electrode was

greater than that of the film at the working electrode. An Ag/AgCl (sat. KCl) reference electrode was utilized to control and modulate the electric potential applied. Electric potential was applied to SNO using a Solatron 1260A electrochemical analyzer in either a constant field for a period of time to induce potentiostatic doping or ramping field over time to study linear sweep voltammetry and cyclic voltammetry.

2.3 Property Modulation in SNO films upon doping

In order to properly assess the structural and electrochemical changes occurring to the SNO thin films upon application of an electrical bias, it was important to first implement a series of tests to ensure no reaction occurred with the water and oxide film. In the case of many electronic materials, exposure to water can significantly modify the material properties by itself [46], especially harsh salts such as KOH or NaCl are dissolved. After baseline tests were performed, systematic testing of different processing parameters such as time, magnitude, and sign of applied bias were undertaken and correlated with changes in electrical resistivity and visible optics. This set of studies aims to determine a baseline understanding of the processing-property relationship for the doping phenomena as it relates to the water-mediated phase transition.

2.3.1 Absence of Externally Applied Fields

As films were to be treated in a water environment, it first became necessary to perform baseline experiments to determine if SNO reacts with aqueous salt solutions under ambient conditions. Figure 2-4 shows the first set of experiments, which entail simply a pristine SNO thin film tested once before and once after being submerged in 0.6 M NaCl for 24 hours. As observed

by both the resistivity vs. temperature plot and its derivative, there are not significant changes to the thin film electrical properties. From this, one can infer that there are no changes to the film within a 24 hour timeframe, so as long as water based experiments are performed in under 24 hours, no significant effects can be attributed to effects such as corrosion in the salt water. The small difference in the overall resistance between pristine and water exposed can be attributed to differences in the electrode area of the Pt paste electrodes. The important distinction here is that the MIT does not change, and therefore the film quality is not changing dramatically, if at all.

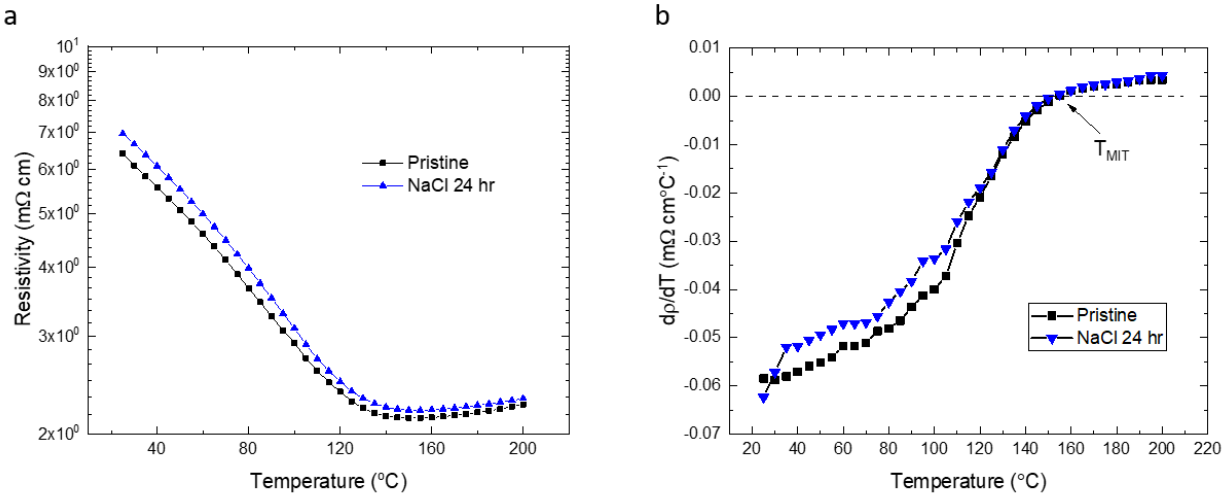

Figure 2-4 Temperature dependent plots comparing effects of NaCl solution exposure as a function of (a) resistivity and (b) the derivative of the resistivity highlighting a metal-insulator transition.

Additional tests were performed to look at the robustness of SNO in a variety of aqueous environments. Figure 2-5 shows the resistance change over time for SNO films exposed to basic and acidic environments. Both show little-to-no change in electrical resistivity as a result of

exposure to the solutions. If the film was etching in these environments, resistivity would be expected to increase as the film thickness would be decreasing (it was assumed to be constant for the measurements here).

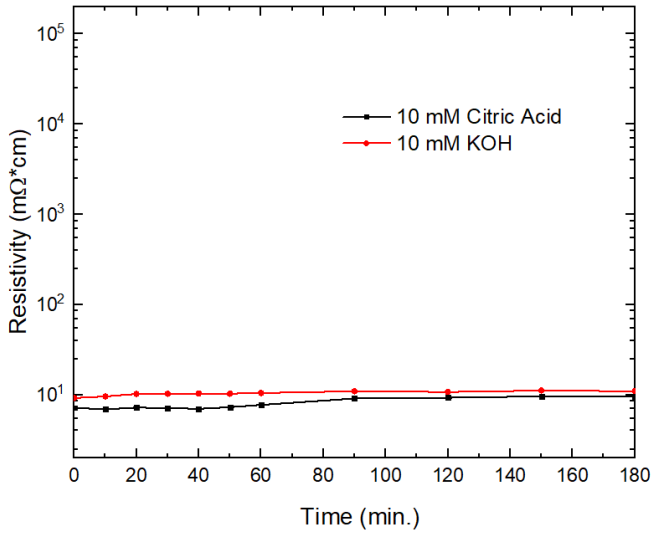

Figure 2-5 Stability of SNO during acidic and basic exposure

A final test showing the pH dependence of the open circuit potential between SNO thin films and an Ag/AgCl reference electrode is shown in Figure 2-6. Error bars show the standard deviation of the measurements. The open circuit potential (V_{OC}) decreases monotonically with increasing pH. This linear relationship between proton activity (and the corresponding surface adsorption) and V_{OC} enables SNO to operate as a pH sensor. It should be noted that this is a reproducible effect and the open circuit potential (V_{OC}) only occurs when the film is in the solution and connected electrically to the reference electrode. Thus this effect is only in response to changes in the solution pH and no permanent effects are observed in the film after removal from the solutions.

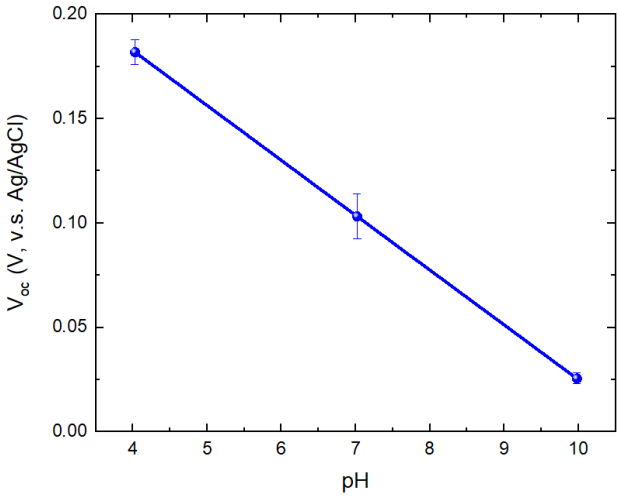

Figure 2-6 (a) pH dependence of the open circuit potential (V_{OC}) for SNO films tested in different buffer solutions.

2.3.2 Processing Variation through the Manipulation of Doping Parameters

The application of an electrical potential in the presence of aqueous solution allows for considerable changes to the properties of SNO thin films. This bias acts as a driving force to intercalate protons and induce the water-mediated phase transition, and modify the band structure in a similar fashion to that of the gas doping methods described in Chapter 1. As the working electrode in the 3-probe cell configuration, the notation in the following chapters corresponds to a negative potential (e.g. -4.0 V) indicating the SNO film having a negative charge relative to the reference electrode. Figure 2-7 shows the change in electrical resistivity of SNO after applying negative electric potentials up to -4.0V for 30 seconds (versus an Ag/AgCl reference electrode) in 0.6M NaCl solution. Upon application of the negative electric potential, the electrical resistivity

of SNO exhibits an increase of more than five orders of magnitude. There is also an observed correlation between the magnitude of the applied bias (from -0.5 to -4.0 V) and the change in resistivity indicating that a higher magnitude of bias causes a larger amount of doping. Application of a positive bias in this manner does not significantly change the resistivity of the film.

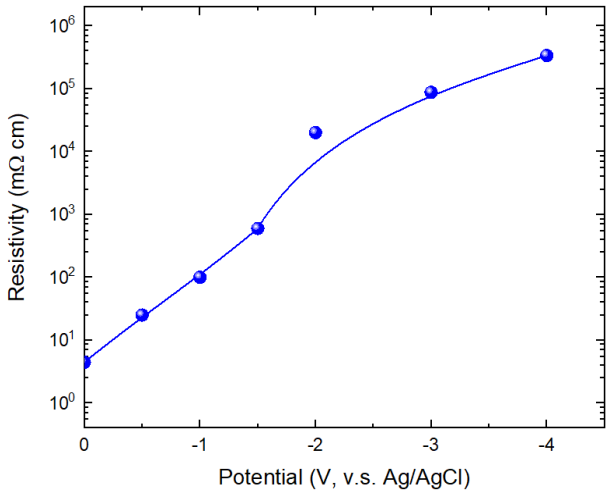

Figure 2-7 Resistivity change in SNO thin films for different biases.

In addition to the resistance changes, thin film optical modulation is observed during the phase transition doping process. Figure 2-8 shows different optical images of SNO thin films grown on Si/SiO_2 and their corresponding biases used to achieve the given state. Similar to Figure 2-7 with the resistance changes, optical modulation appears to be related to the magnitude of bias with which the film was treated. Samples grown on LAO also showed optical modulation; these epitaxially grown samples turned from opaque to transparent upon doping.. At this time, it is uncertain what causes the blueish color observed in the polycrystalline SNO samples grown on Si/SiO_2 and shown in Figure 2-8. It may be due to many factors such as light scattering at the grain

boundaries, impurity phases in the thin films (e.g. non-stoichiometry of Sm and Ni), or perhaps even some interaction between the substrate SiO_2 layer and the SNO.

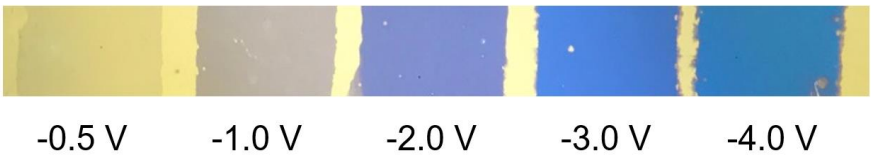

Figure 2-8 (a) Optical modulation accompanying phase change.

Figure 2-9 shows that this doping process and phase transition are reversible. This figure compares the resistivity vs. temperature change for pristine and water-treated SNO/SiO_2/Si samples. Ultimately, it shows a resistivity change of several orders of magnitude with a negative bias applied to the film, followed by a return to electrical properties mostly similar to that of the original film with a positive bias. Additionally, the doped film shows a smooth decrease with increasing temperature indicating an insulating state with localized electrons and non-volatility. This newly observed state occurs regardless of the salt used to produce the aqueous solution (e.g. KOH, NaCl, citric acid).

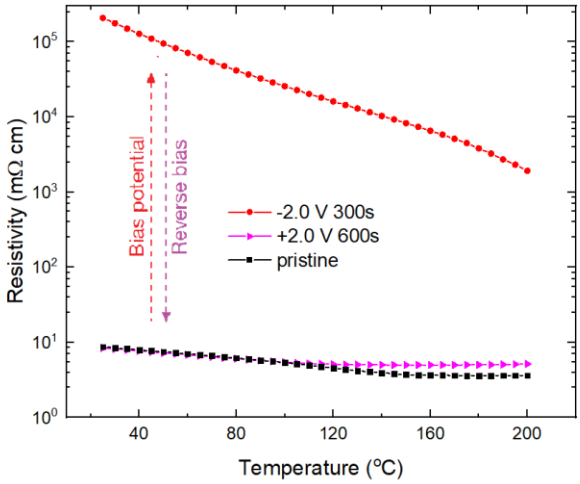

Figure 2-9 Resistivity vs. temperature showing reversible phase transition.

Much of the previous discussion focused upon the magnitude and sign of the bias applied to the oxide film. However, if the magnitude and sign are kept constant, but instead the time is modified, similar effects to resistivity change are observed. Figure 2-10 shows one such case where the same sign and magnitude of bias are applied, but for different amounts of time. As expected, the longer the bias is applied, the greater the change in resistivity of the SNO film indicating that the degree of doping is a function of the bias applied and also the amount of time it is applied for. Furthermore, Figure 2-10 shows that changes in the electrical properties of water-treated SNO is non-volatile in ambient conditions, at least for 120 minutes. Ultimately, this shows doping effects are not simple electrostatic field effects induced by charge accumulation at the surface, but instead a water-mediated phase transition.

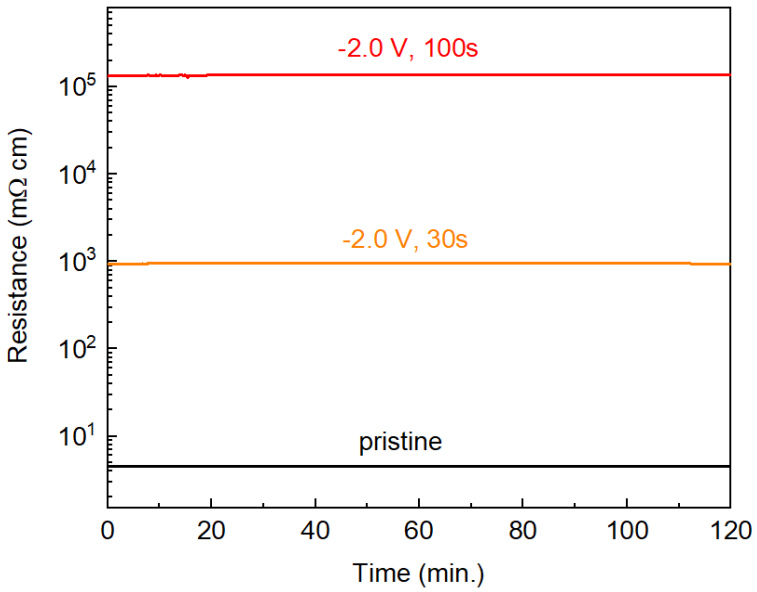

Figure 2-10 Non-volatility of phase transition applied over different time periods.

In summary, there are different processing parameters that determine the degree and rate at which this reaction proceeds. Here, magnitude and sign of electrical bias as well as time of application were all examined as well as their effects on the SNO thin film. When in the presence of an aqueous solution and an externally applied electric field, SNO thin films respond with changes in electrical and optical properties. Due to the fact that it changes the properties in a similar fashion to the alternative gas-doping methods [11], [19], this water-mediated phase transition can be attributed to proton (or possibly other cation) intercalation from the water in the following simplified chemical reaction:

$$2\,SNO\,(s) + H_2O\,(l) \leftrightarrow 2\,HSNO\,(s) + \frac{1}{2}O_2\,(g)$$

In this equation, it is understood that HSNO is significantly more resistive its SNO counterpart and an electrical bias can be used to push the reaction either way. With regards to charge transfer is this process, oxygen is produced at the graphite counter electrode in the 3-probe cell, and electrons travel through the externally applied circuit and recombine in the working electrode and charge balance the intercalated protons. Together, these results indicate a strong relationship between treatment conditions of the nickelate film and the properties observed in the film. Further chapters will look more in-depth at some of the kinetics of the doping process as well as the overall effects upon the film structure.

It is worth noting here that at elevated temperatures, the resistance will slowly return to pristine conditions. This is a thermally activated process by which the hydrogen leaves the lattice under atmospheric conditions. As such, it is unlikely that proton doped samples stored under ambient conditions would remain highly resistive for long periods of time. In order to increase the time for which they may be stored, it may be useful to add a H^+ - blocking layer such as SiO_2 to cap the sample and preserve the highly resistive film.

3. EFFECTS OF MODIFIED FIELD FUNCTION ON DOPING

3.1 Principles of Cyclic Voltammetry

Common electrochemical characterization of charge transfer processes utilizes a three-probe setup to determine rate-limiting kinetics. This form of voltammetry utilizes a triangle wave function over time instead of a stepwise function like the potentiostatic bias applications utilized in chapter 2. Figure 3-1 shows a comparison of the two methods and expected results for each.

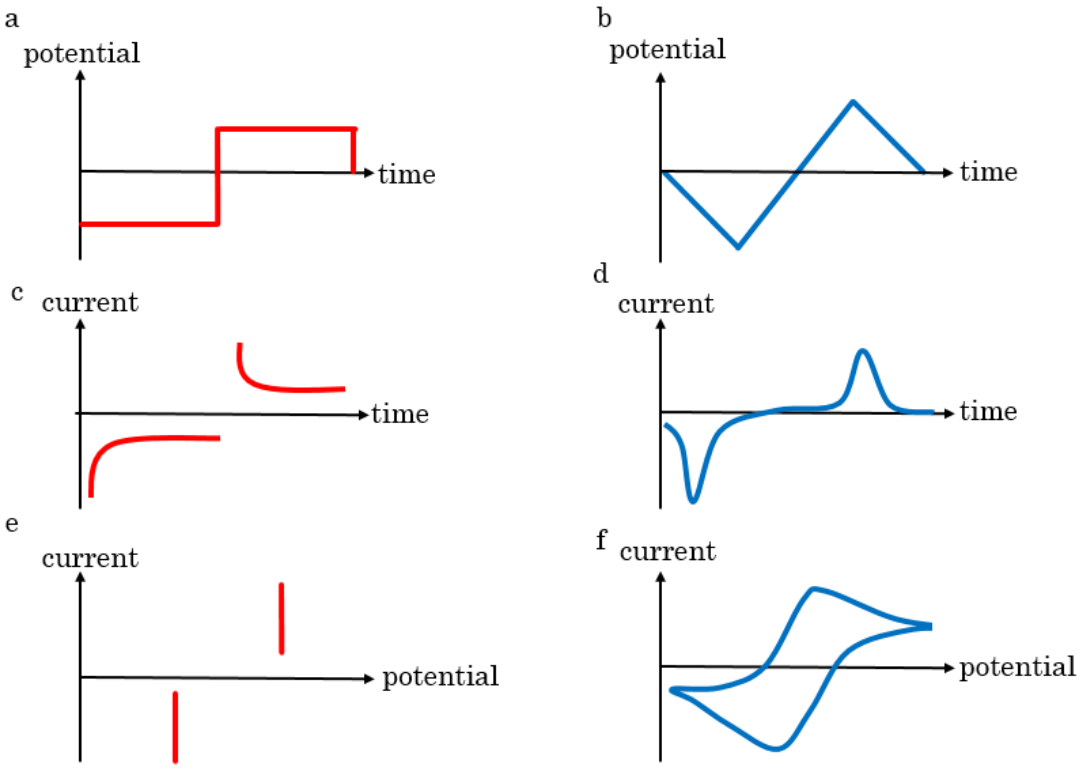

Figure 3-1 Comparison of (a, c, e) potentiostatic and (b, d, f) sweeping voltammetry and the expected relationships between the different methods.

As observed in Figure 3-1, potentiostatic testing may not be as useful for determining kinetic relationships between important points in the doping process such as the maximum potential where a maximum charge transfer occurs. However, this type of information can be obtained from sweeping voltammetry and is useful for characterizing an unknown chemical reaction. A cyclic voltammogram plot as seen in Figure 3-1(f), contains much information about the redox charge transfer processes, specifically the charge transfer rate and limits to what is transferring. Relative charge transfer rates, reaction reversibility can be determined from a cyclic voltammogram. If a reaction is deemed to be fully reversible, there will be a very symmetric current vs. voltage plot, indicating charge transport in the chemical reaction is limited by the rate of mass transfer [47]–[49]. Symmetric in this case indicates similar height and area under both the anodic and cathodic curves as well as a small potential difference (ΔE) between them (~59mV/e^-). However, if the voltammogram is not symmetric, the reaction would be deemed either quasi-reversible or irreversible. Quasi-reversible reactions occur when there is some abnormality in the reaction kinetics, even if the reaction appears to reverse [48], [50]. Figure 3-2 shows a comparison between a fully reversible and quasi-reversible reactions when scan rate is varied. Typically quasi-reversible reactions occur when there is competition between the electron transfer and mass transfer for which will rate-limit the chemical charge transfer reaction. Irreversible reactions occur when either only an anodic or cathodic peak appears and not its corresponding partner on the reverse process. Irreversible and quasi-reversible reactions are easily distinguished from fully reversible reactions by changing the scan rate and looking at how the voltammogram changes. The voltammogram will change significantly with scan rate if electron transfer is the kinetically limiting step [48], [50].

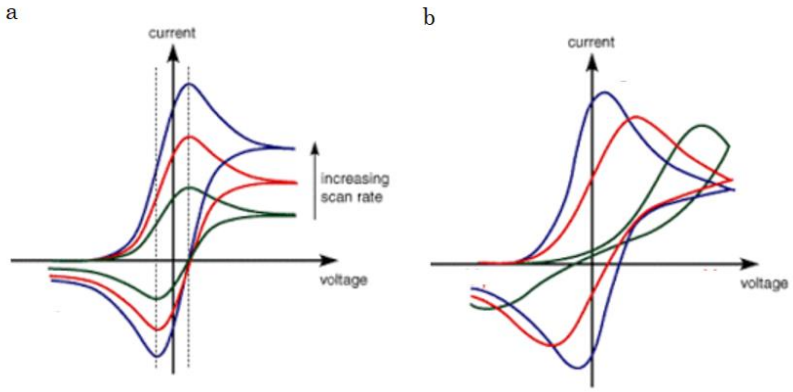

Figure 3-2 Cyclic voltammograms highlighting the difference between (a) reversible reactions and (b) quasi-reversible reactions when scan rate is changed. Adapted from [50]

3.2 Sweeping Voltammetry of Samarium Nickelate

In the following sections, cyclic voltammograms are used to describe the behavior SNO thin films on aqueous solutions and will be analyzed for information regarding the phase transition process. A typical cyclic voltammogram for SNO in 10 mM NaCl with a scan rate of 1mV/s from +0.25 V to -1.5 V to +0.75 V and back to +0.25 V (vs. Ag/AgCl) is shown in Figure 3-3.

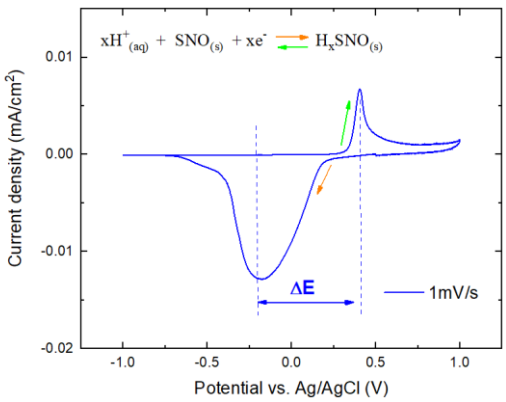

Figure 3-3 Cyclic Voltammogram of SNO in 10 mM NaCl.

Analysis of this voltammogram can tell us much about the interaction between the SNO film and the water during the bias application. One of the first things to take away from this plot is that a large charge transfer occurs around -0.2 V. This large cathodic peak indicates significant charge transfer and corresponds to the intercalation of H^+ into the crystal structure. In order to maintain charge neutrality, electrons are also added to the film, but during this process, they move into the graphite counter electrode and recombine within the SNO film. During the process, for each H^+ added, one Ni^{3+} reduces to Ni^{2+}. This change in Ni valence is part of the reason for the large resistance modulation upon doping as the phase transition occurs. It is noteworthy that the oxidation peak matching to the de-intercalation process (seen at roughly +0.4 V) is significantly smaller in both peak current, as well as total area under the curve. This indicates that less charge overall is transferred during this reverse part of the reaction, or that the back reaction is limited in some way. Furthermore, this asymmetry suggests that the overall reaction is quasi-reversible, an observation which is reinforced by the large distance between the two peaks ($\Delta E > 0.6$ V) corresponding to this chemical reaction. Thus, this reaction is not mass transfer limited, or the protons intercalating are not the rate-limiting step in this chemical reaction. Instead, the mass and electron transfer are at the very least on the same order of magnitude. However, as the film becomes more insulating, it is possible that the reversibility of the reaction is hindered by the rate of electron transfer through the resistive SNO. One important note regarding the voltammogram for SNO is that the film quality (polycrystalline, degree of crystallinity, impurities) will affect the output. All the voltammograms presented in this chapter are polycrystalline SNO samples on Si/SiO_2 substrates. SNO/LAO samples will be examined later and they show slightly different qualities.

3.2.1 Effects of Solution on Voltammetry

Interesting changes to the voltammogram occur modifying the aqueous solution used to induce the phase transition. Figure 3-4 shows different linear sweep voltammograms of SNO in both basic and acidic solutions. Linear sweep voltammetry is similar to cyclic voltammetry in that it is a directional sweep, however, it is simply a singular directional sweep as opposed to cyclic, triangular functions of voltage application where the sign of the applied bias changes (there is no reverse bias).

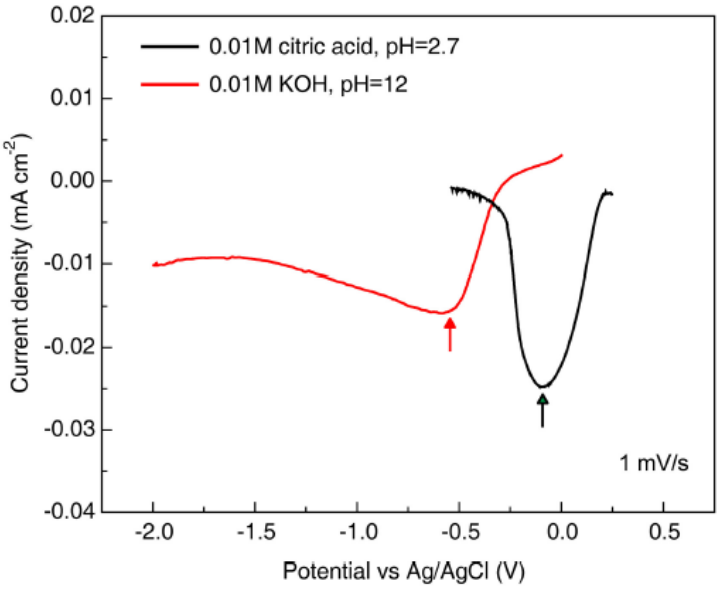

Figure 3-4 Linear sweep voltammetry comparing SNO in basic and acidic solutions.

Comparison of the different solutions indicates the doping process is directly related to the pH of the solution. The primary differences between the two curves is the shift in peak position, which points towards the concentration of hydronium ions (H_3O^+) influencing how readily the reaction will occur. The influence of the H^+ concentration on SNO doping thermodynamics agrees

with the greater context of the overall chemical reaction. In general chemistry, a reaction in equilibrium will shift towards the products side if more reactants are present and vice versa. Thus, by increasing the concentration of H^+ in solution (lowering pH), a reaction that consumes H^+ will be more energetically favorable. In this case with the proton doping of SNO, by lowering the pH of the solution, it takes less energy to drive the H^+ into the lattice. Figure 3-4 shows the citric acid solution utilizing a lower driving force to start the cathodic intercalation process (cathodic peak = -0.1 V).

This set of results is also in good agreement with those shown in the pH dependence vs V_{OC} of Figure 2-6. Figure 2-6 shows that there is a larger, positive open circuit potential for lower pH solutions. This larger positive open circuit potential is a natural driving force for the intercalation of protons into the lattice.

Other, minor differences exist between the basic and acidic curves such as the overall background slope between the end points of the scans, but these are due to differing conductivities of the solutions. Citric acid is a weak acid and much less conducting when compared to KOH, a strongly dissociating base.

3.2.2 Scan Rate Dependence on Doping

A more thorough examination of this quasi-reversible H^+ intercalation into SNO can be observed by adjusting the scan rate and looking at the underlying electrochemistry. Figure 3-5 shows how changes in the scan rate of SNO affect the voltage vs current plot for a series of voltage sweeps in citric acid.

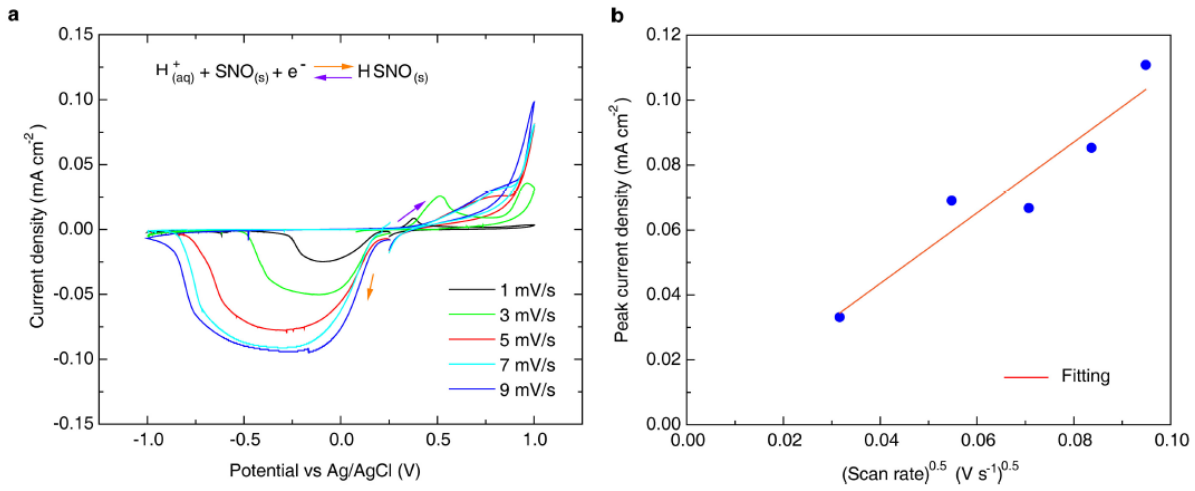

Figure 3-5 (a) Scan rate dependence of current vs. potential for SNO in citric acid and (b) fitting to the modified Randles-Sevcik equation.

Aside from the obvious peak asymmetry between the cathodic peak (intercalation at negative potentials) and anodic peak (de-intercalation at positive potentials), the shifting of the peak position with respect to scan rate indicates clear quasi-reversible behavior and an electron limited charge transfer process. At scan rates faster than 9 mV/s, the anodic peak is not fully visible as the oxygen evolution reaction begins to become visible as a sharply rising peak. If the scan were to continue outside these constraints, this would be the primary observable phenomena as it continuously ramp up as more oxygen was produced for higher currents (or hydrogen at the positive potentials).

By changing the ramp rate of the applied potential, the kinetics of the charge can be characterized by a modified Randles-Sevcik equation as shown below, which relates cathodic current density (I_P/A) to the square root of the scan rate ($\nu^{0.5}$). The results for these comparison are plotted in Figure 3-5 (b) [47], [51].

$$\frac{I_p}{A} = 2.99 \times 10^5 \, n(\alpha n_a)^{0.5} C (Dv)^{0.5}$$

In this equation, C is the H^+ concentration of the solution in mol/mL; D is the diffusion coefficient of protons in SNO; v is the scan rate; n is the number of electrons exchanged in the reduction process, which is unity because it corresponds to the reduction of Ni^{3+} to NI^{2+}; n_a is the number of electrons transferred in the rate limiting step, which is also taken as unity because there is only a single step in the proposed reaction; and a is the charge transfer coefficient, which can be approximated to 0.5 [51]. From the slope of the plot, D can be calculated to 3.6 cm^2/s at room temperature. This result is in very good agreement with AIMD simulations which calculate the value to 6.0 cm^2/s [5]. This relatively close agreement between the two values give credibility towards the other assumptions used in the equation (n, n_a, and a values) and indicate that the stoichiometric relationship between SNO and its proton-intercalated form is approximately one H^+ per Ni^{3+}.

4. STRUCTURAL CHANGES IN SAMARIUM NICKELATE

4.1 Introduction

In the previous chapters, process-property relationships as well as electrochemical characterization of doping induced SNO phase transitions have been examined. Although these characterization techniques give a rough idea regarding the overall effects of the doping upon the material properties and kinetics, the results do not complete a full picture encompassing the overall effects the nickelate thin films experience during water-mediated proton doping. Here, structural implications of the doping methods – both potentiostatic doping and linear sweeping scans – will be examined in detail to better understand how the proton intercalation process affects the structure of the SNO.

4.2 X-ray and neutron scattering

The characterization methods used in this work to study proton doping of SNO include both x-ray and neutron elastic scattering techniques. For x-ray scattering, both x-ray diffraction (XRD) and small angle x-ray scattering (SAXS), also known as x-ray reflectometry (XRR) are used. For neutron scattering, neutron reflectometry was used. These techniques all use the Bragg-Brentano geometry. In general, x-ray diffraction uses atomic scattering and detection at higher 2Θ angles to measure planar spacing in a crystal lattice. Both 2Θ and Q – space are referenced in this work, and the two are interchangeable. Q – space is independent of the radiation type, where 2Θ takes into account the radiation used for data collection (Q_z denotes momentum transfer orthogonal to the surface of the specimen).

In contrast to XRD, XRR and NR measure the overall thickness of the film and therefore use very low angles for detection. In addition to measuring the film thickness, reflectometry techniques are able to gather some information on the film density and roughness. The utility of having two different reflectometry techniques allows for contrast between different types of elements. X-ray and neutron beams each 'observe' atoms with distinct cross sections, but the cross sections are different for each beam as highlighted in Figure 4-1 [52]. This is of paramount importance for studying proton intercalation as H^+ is more or less undetectable to x-ray measurements which focus on electron density. These measurements can only indirectly observe the effects H^+ has on the film by probing the surrounding structure. Conversely, neutron measurements probe the atomic nucleus and are therefore more sensitive to light ions such as H^+. As such, both reflectometry measurements will be useful in the study of SNO structure.

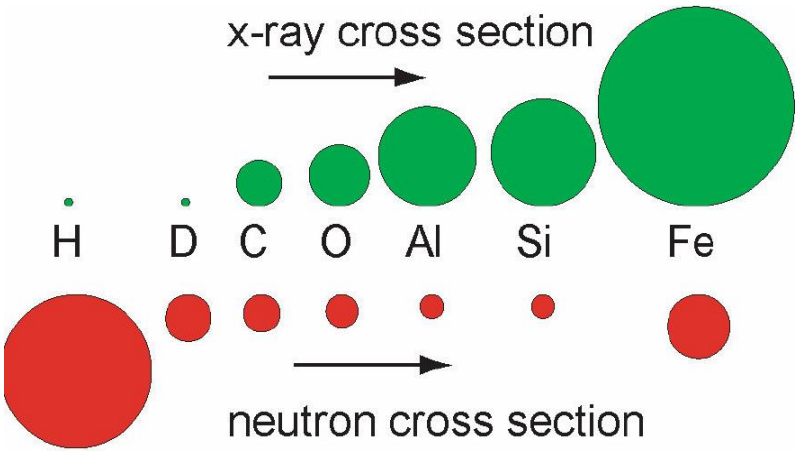

Figure 4-1 Atomic cross sections for x-rays and neutrons adapted from [52].

4.3 Structural changes during potentiostatic doping

The goal of set potential-time experiments is to determine start and end points of the doping process and compare pristine and hydrogenated states. In this section, before and after snapshots will be explored study the differences between the as-fabricated SNO films and their water treated counterparts.

4.3.1 X-ray Diffraction

XRD is a suitable tool for materials analysis in quantifying changes in crystal structure for different films. Figure 4-2 shows the crystal structure of a SNO/LAO thin film before and after the hydrogenation process from treatment in a 10mM KOH aqueous solution at – 4.0 V for 30 s. From the wide range full 2Θ scan (Figure 4-2a), it is apparent that there are no significant changes to the crystal structure such as new phases appearing, a common occurrence observed in other oxides such as cobaltites upon exposure to water [53]. From the Synchrotron XRD curves (Figure 4-2b), it can be seen that the (220) peak of pristine SNO (orthorhombic notation) appears at $Q_1 \approx 3.29$ Å^{-1} as a shoulder with slightly lower scattering vector Q_z than that of the LAO (002) diffraction peak (Pseudocubic notation), demonstrating the epitaxial growth of SNO on LAO. After water treatment, the epitaxial relationship of SNO on LAO is preserved. Peak 1 shifts to a lower $Q_z = 3.11$ Å^{-1}, which corresponds to an increase in the lattice constant by 5.7%. Thus, there is significant film expansion as protons from the water are incorporated into the lattice during this doping process.

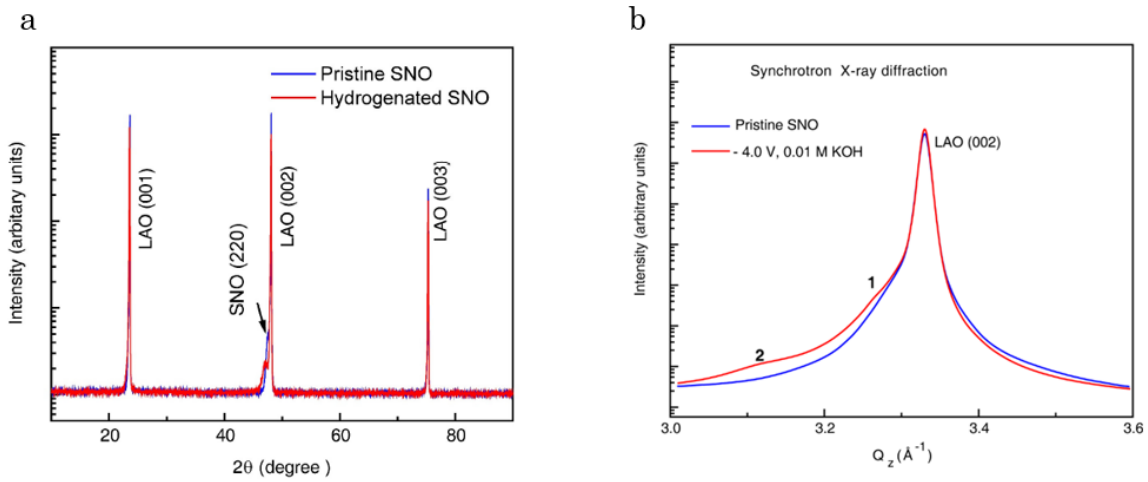

Figure 4-2 X-ray Diffraction of pristine and hydrogenated SNO for (a) wide range 2Θ and (b) synchrotron zoomed in on the SNO (220) peak

4.3.2 X-ray Reflectometry

Additional examination of the film structure, specifically looking at the out of plane momentum transfer and therefore thin film expansion as a whole was performed using XRR. Figure 4-3 shows XRR of the same SNO/LAO sample spot treated in different areas with different salt solutions. Notably, 10 mM KOH and 10 mM citric acid were used for treatment to examine the role of different cations in the doping process. It is unlikely that a cation as large as the citrate ion would be able to intercalate into the film, but it has been observed in other studies that larger cations such as Mg^{2+} can intercalate into SNO thin films [11]. From the very similar film expansion highlighted in Figure 4-3b, it can be inferred that no significant changes occur to the film when doping with a solution containing other ions (such as K^{+}). Recall, Q-spacing is related to 2Θ, and therefore oscillation frequency is directly proportional to film thickness. Therefore, as the film is treated and the XRR oscillation period decreases, the film is expanding. This is consistent with the

XRD results. Furthermore, similar film expansion is observed with both KOH and citric acid solutions indicating a general mechanism to the phase change of SNO in various aqueous media. This is important because the salt is necessary to provide conductivity and enable the water to denature into protons to enter into the film. Thus, this process generally occurs regardless of what salt is used.

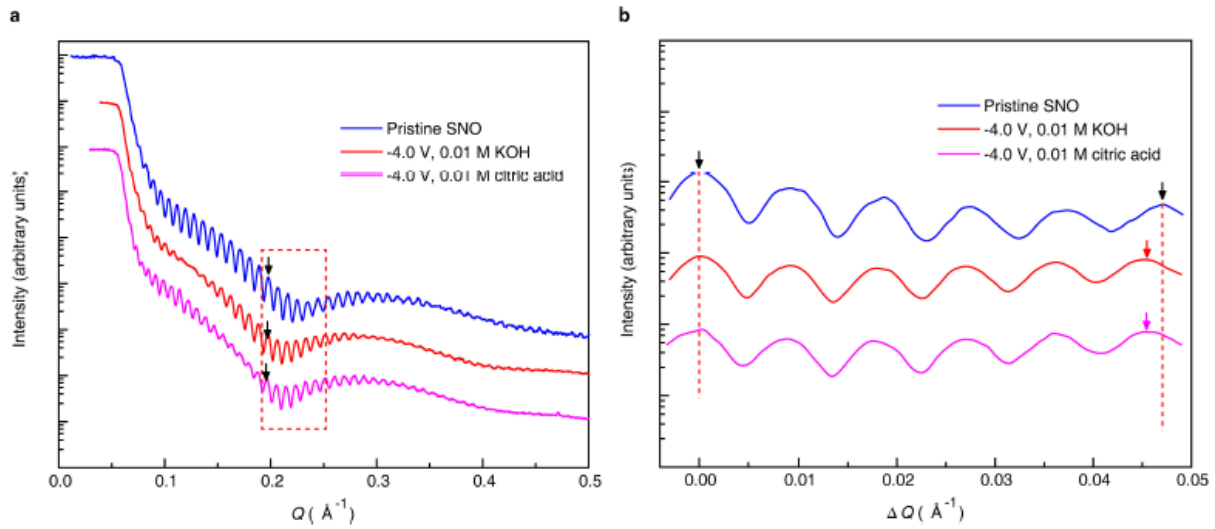

Figure 4-3 X-ray Reflectivity of SNO/LAO thin films highlighting the similarities with treatment using different salt solutions for (a) full Q scan and (b) normalized Q scan highlighting peak shift.

XRR was also used to examine the sequential nature of the doping process. Figure 4-4 highlights the subsequent applications of a bias to the film. Again, similar to previous structural characterization results, the film expands upon treatment. However, in this case, sequential treatments are used and as expected, the film expands in a proportionally sequential nature. Figure 4-4b shows the normalized oscillation period shift and how the peaks move qualitatively and incrementally in the doping process as the film expands directly in response to the bias applied.

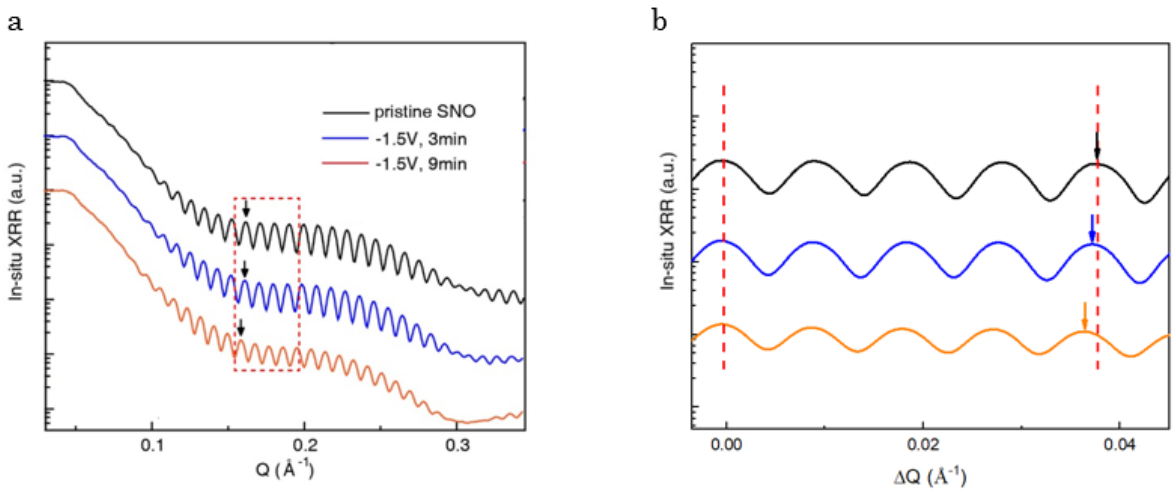

Figure 4-4 X-ray Reflectivity of In-situ SNO treated with subsequent bias experiments (a) full scan and (b) normalized region highlighting film peak shift

4.3.3 Neutron Reflectometry

Neutron Reflectometry (NR) was used here to further study on the proton doping process because of the unique sensitivity of neutron scattering to the differentiation small ions and isotopes such as H^+ and D^+. In the NR experiments, it was necessary to use larger substrates such as Si/SiO_2 because there is a relatively low flux off the neutron beam relative to an x-ray beam. Thus, the amount of data collected is a function of the surface area exposed to the beam and the amount of time for data collection. Therefore, to maximize beam time efficiency, larger samples were developed and the doping process tailored to achieve more uniform doping. If samples were non-uniformly doped, the data from the beam would not be worth much because the reflectivity scattering vectors for different film thicknesses would be added together, the signal would wash out, and it would be impossible to discern the meaning of the data analytically.

SNO/SiO_2/Si thin films of pristine and treated in H_2O and D_2O KOH solutions respectively. Due to the large nature of the samples required for the neutron scattering experiments, different heat treatments were necessary for each sample. Both samples were grown in the same deposition process, but annealed separately. As such, it can be expected that there may be some sample to sample variation. The raw NR data shown in Figure 4-5 indicates a qualitative film expansion similar to that observed in the XRR results indicating that the film expands regardless of isotope in the aqueous solution.

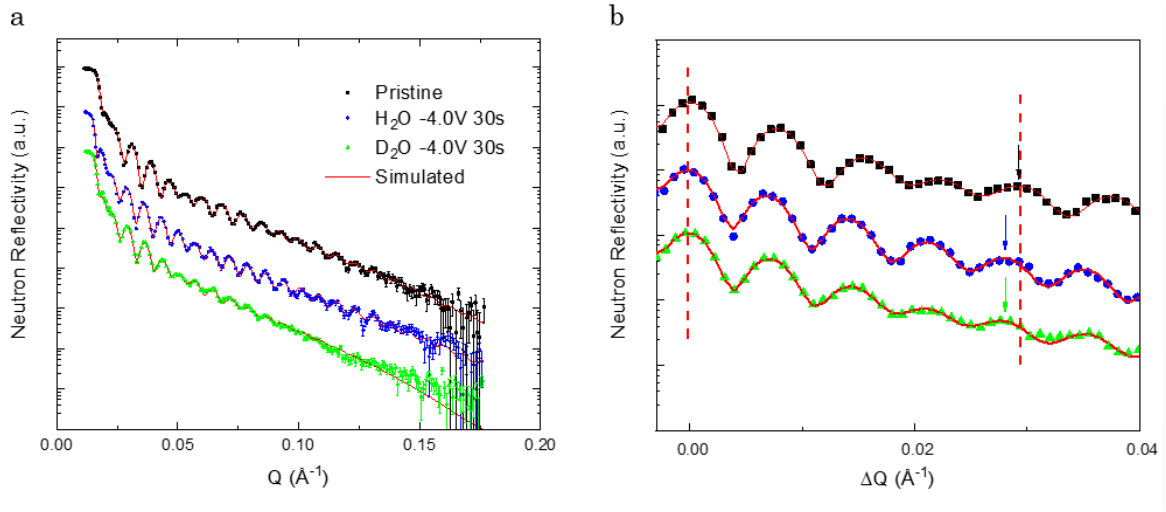

Figure 4-5 Neutron Reflectivity of SNO treated with H_2O and D_2O (a) full scan with simulated data fit and (b) normalized region highlighting film similar peak shift

This NR data was simulated and fitted using the NIST Refl1d software package [54] and the process is described briefly in Appendix A. Figure 4-5 shows relatively good agreement between the final fits obtained and the experimental data. Figure 4-6 is the scattering length density (SLD) models which are built in the fitting program. Average SLD is the sum of the scattering lengths per unit volume. In other words, it is the density the neutrons 'observe' the

film as. A higher SLD indicates that there are more elements with a large neutron cross section that are tightly packed in a smaller volume.

The SLD profiles in Figure 4-6 show interesting effects that are consistent with other experimental results of this section. Namely, when comparing just the Pristine and H_2O treated films, it can be seen that there is ~6.9% film expansion. Furthermore, the SLD decreases overall, which can be due to two effects. First, the film is expanding, which represents a re-organization of the existing thin film mass. Thus, the same number of atoms are distributed over a larger volume, obviously leading to a decrease in SLD. Second, there is additional H^+ in the film, which will decrease the overall SLD. The other critical observation from this data is that there is a difference between the two treatments. The isotopic contrast manifested itsself during the fitting process and shows (as expected) that the D_2O film has a higher SLD than the H_2O treated film. Most evidence up to this point has been observations of the effects of protons on the SNO film structure, but this is direct evidence that there are protons doping into the SNO thin film.

One additional important note regarding the SLD profiles shown in 4-6 is with respect to the surface SLD. All three profiles show a small layer with increased SLD at the surface. None of the models used to fit were even close to matching the data without this layer included directly on the surface. This surface layer is likely NiO or some other such oxide present from the annealing process that is on the surface of the film. In later experiments, the samples were treated with a brief HCl etch to remove any such residual surface oxide.

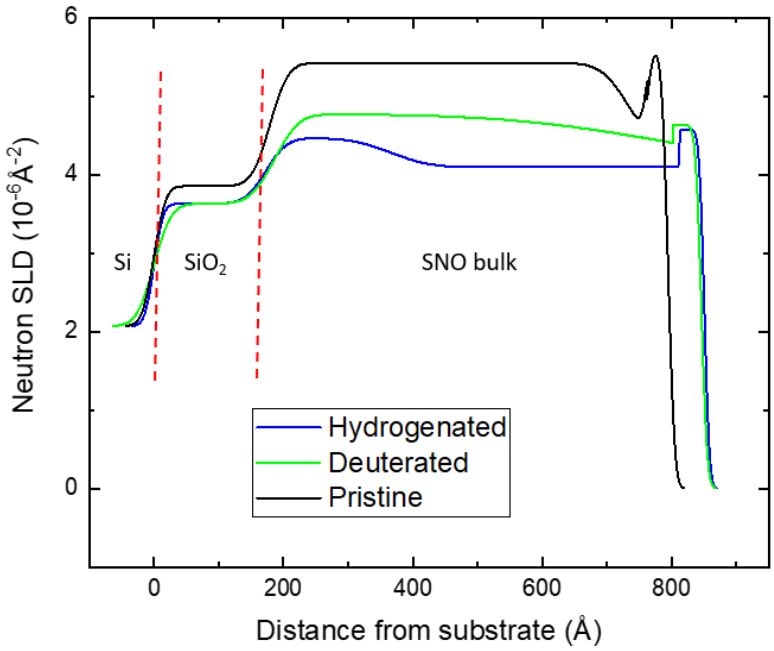

Figure 4-6 Comparison of neutron scattering length density (SLD) profiles of the SNO films treated with H_2O and D_2O solutions. Profiles are simulated best fit models from the neutron data in Figure 4-4.

4.4 Structural changes during Cyclic Voltammetry

In contrast to the structural characterization of the potentiostatically induced phase transition studied in the previous section, studies were also performed at points of interest during a cyclic voltage sweep of SNO. A representative SNO/LAO cyclic voltammogram is shown in Figure 4-7 with marked points of interest that will be referenced in the following section: A – pristine; B – partially hydrogenated; C – fully hydrogenated; and D – partially dehydrogenated. It should be noted that this voltammogram appears mostly similar to those examined in the previous section with respect to disparity between cathodic to anodic peak ratios, even if the plot appears somewhat different. The differences are likely the result of differing film qualities arising from polycrystalline and epitaxial growths.

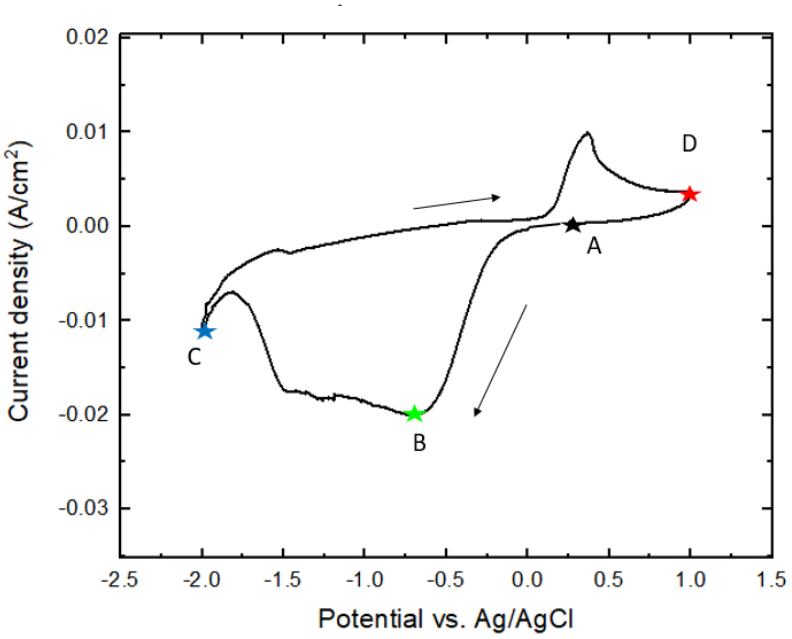

Figure 4-7 Current vs. Voltage voltammogram for SNO/LAO with marked points of interest.

4.4.1 X-ray Diffraction

Juxtaposed to the previous XRD section only characterizing the doped and un-doped SNO film, here we examine different points along the way as the protons move into and out of the SNO lattice. Figure 4-7 a shift in the (220) SNO peak indicating lattice expansion, similar to that observed in the previous section. However, the diffraction patterns here highlight not only the shift and consequent film expansion during the hydrogenation process as the SNO film is doped, but also the consequent film contraction as the film loses protons during the dehydrogenation process.

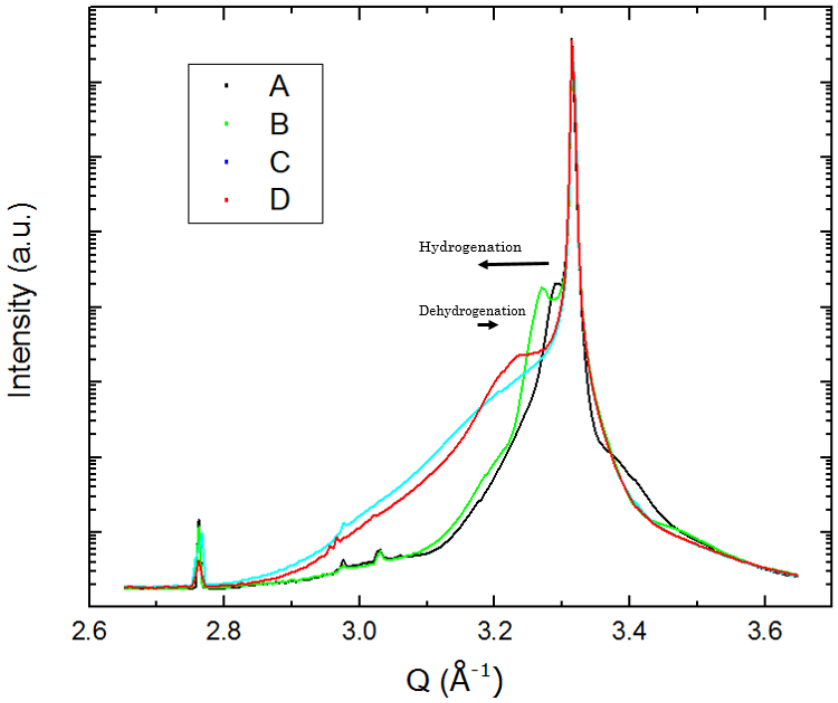

Figure 4-8 XRD corresponding to points on the cyclic voltammogram highlighting the film 'breathing' during the hydrogenation and dehydrogenation processes.

4.4.2 Neutron Reflectometry

Neutron reflectometry was further used in conjunction with the cyclic voltammetry in order to establish if the doping kinetics occur mainly at the surface or if it is a bulk phenomenon. Figure 4-9 shows neutron reflectivity data and associated fits. It is understood that H^+ has a lower SLD than the bulk of SNO and when incorporated into the lattice, it will lower the overall observed neutron SLD value. Thus, the most obvious observation from the data is that protons are indeed being incorporated to the film during the doping process similar to the potentiostatic experiments. It should be also noted that, as discussed in section 4.3.3, the film expands upon

doping, there may be some rearrangement of existing Sm, Ni and O ion density as the host lattice expands to accommodate the dopants, which will also decrease the SLD.

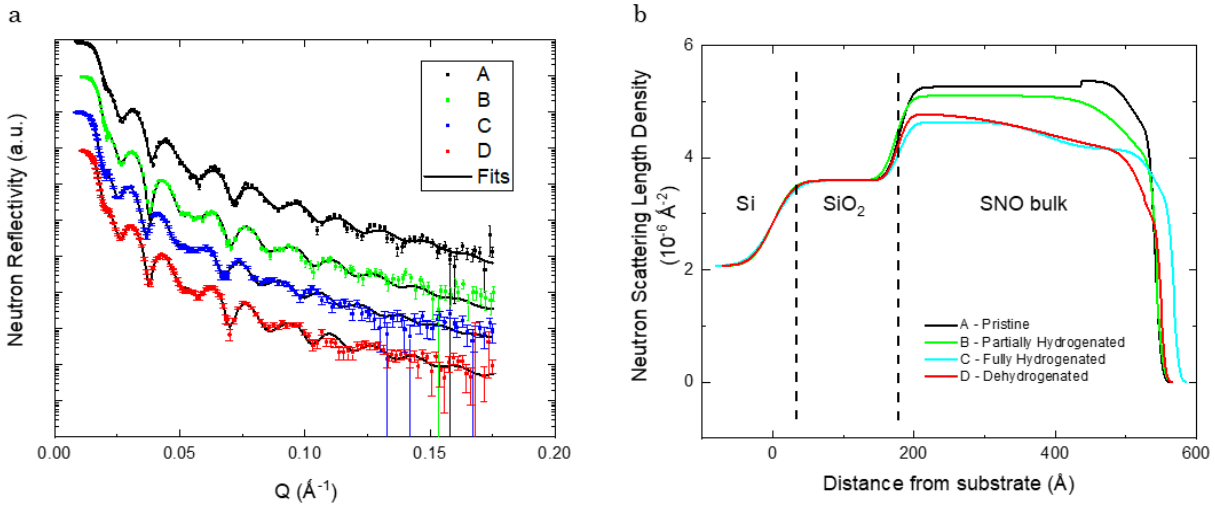

Figure 4-9 (a) NR raw data and simulated fits and (b) Calculated SLD profiles for points of interest on the cyclic voltammogram of SNO

From the fitted data profiles in Figure 4-9b and calculated dopant concentration it is observed that with partial protonation of the film (point B), the film does not expand significantly. This is in agreement with the lattice parameter data of Figure 4-8. Furthermore, a majority of the dopant initially concentrates at the water interface. However, as the doping process progresses, the profile fitting shows that a most of the protons come to be distributed throughout the bulk of the film. This can be seen because the overall SLD of the bulk reduces concomitantly with that of the surface layer. It is further observed that the film expands upon full hydrogenation (point C). Finally, the fit from the dehydrogenation process shows an increase the

overall SLD and a decrease in thickness. This again shows consistent changes in only the bulk of the film and not significant changes at the surface. It should be noted that the decrease in thickness could describe a slight increase in SLD as the Ni and Sm ions are more concentrated.

Overall, it is observed that when they are doped into the film, the protons distribute somewhat evenly in the lattice and do not concentrate at either the SNO-water or SNO-SiO_2 interfaces. With the significant lattice and film expansion upon doping, it is understandable that the dopants self-distribute in order to reduce stress fields within the lattice. As such, the changes to the overall film properties should be mostly uniform. Ultimately, for the doping of SNO thin films, the processing ties closely to the structural and property changes, and modifications the processing method can be expected to concurrently affect the final structural and properties of the film as it is doped.

4.5 Cycling Effects on Structure

The effects of one hydrogenation-dehydrogenation cycle may be magnified over several cycles with respect to the SNO phase-transition process. These effects can also be observed by looking at the structural changes. Figure 4-10 displays NR data and its associated fit for pristine SNO as well as the same sample after one and five cycles. There are a couple observations that can be made from this data. It is obvious that there is some sort of etching occurring after many cycles as the overall film thickness decreases. This data is not easily able to be seen qualitatively from the raw NR data as with some of the other studies (e.g. potentiostatic expansion in XRR). However, with the fits, an overall film thickness decrease is shown for the sample with five cycles. There is also an increase in surface roughness, which can be observed qualitatively in the raw data, which shows dampening of the oscillations more quickly for the

sample with five cycles. Hence, not as much specular data was able to be collected for this sample because the data quality rapidly degraded. Nevertheless, there is some etching in the cycling process, likely during the oxidation at the positive potentials where the hydrogen is removed from the film.

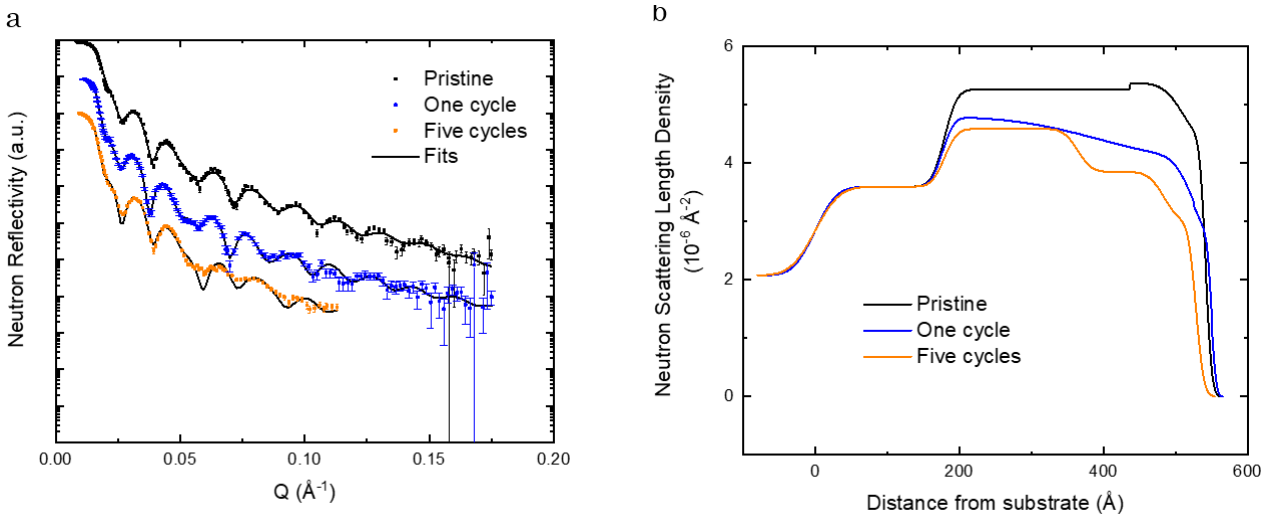

Figure 4-10 (a) NR raw data and simulated fits and (b) Calculated SLD profiles for multiple hydrogenation and dehydrogenation cycles.

4.6 Structure – Processing – Property Relation

One final examination of the structural aspects of the SNO phase transition aims to draw correlations among the structure – processing – properties of the system. Figure 4-12 shows the resistivity change as a function of XRD peak shift for the points of interest in the cyclic voltammogram shown in section 4.4. Noticeably, as the XRD peak shifts (film expansion), resistivity increases. As previously established, the amount of film expansion is related to the

processing (in this case the amount of bias applied). Likewise, the change in resistivity is related to the processing in a similar fashion. This plot confirms the relation between all three aspects, showing there is a correlation between the structure and the properties: as the film expands (from proton intercalation), the resistivity increases (band structure changes).

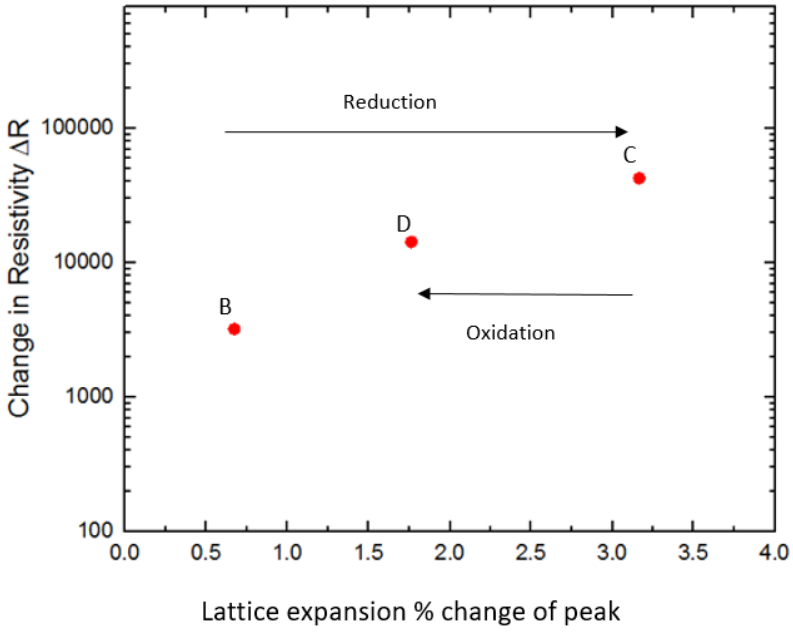

Figure 4-11 Resistivity change as a function of XRD peak shift.

5. VARIATION IN DOPING OF RARE EARTH NICKELATES

5.1 Water-Mediated phase transition of $RNiO_3$

Previous sections of this work have examined in detail the structure-processing and property interrelation of the water-mediated phase transition of SNO thin films. Data has been presented regarding how different applications of an electrical bias in aqueous solutions have enabled correlated changes in not only structure of the lattice and film bulk, but also with regard to the film resistivity and optics. The goal of this section is to incorporate this broader understanding and explore how these structure – processing and structure – property associations change with respect to modifications in the structure brought about by changing the rare earth nickelate ion on the A-site in the $RNiO_3$ lattice.

$RNiO_3$ thin films of $NdNiO_3$ (NNO), $SmNiO_3$ (SNO), and $EuNiO_3$ (ENO) were all prepared using similar processing conditions as the SNO previously studied. Although deposited in separate batched, samples compared in the following figures were all annealed together in order to minimize the variation during the fabrication process as much as possible.

5.2 $RNiO_3$ Trends in Cyclic Voltammetry

Efforts to study the change in the structure-processing connection rely on preparing $RNiO_3$ thin films of different compositions and subjecting them to the same stimulus in terms of salt solution and applied bias. As the primary differentiator for processing conditions in this work, voltammetry was used to observe the effects on $RNiO_3$ thin films. Figure 5-1 shows the respective curves for all three compositions tested. Some trends can be seen when comparing the different

voltage-current curves. Most noticeably, there is a slight shift in the maximum current densitywith respect to A-site substitution as highlighted by the arrows in the chart.

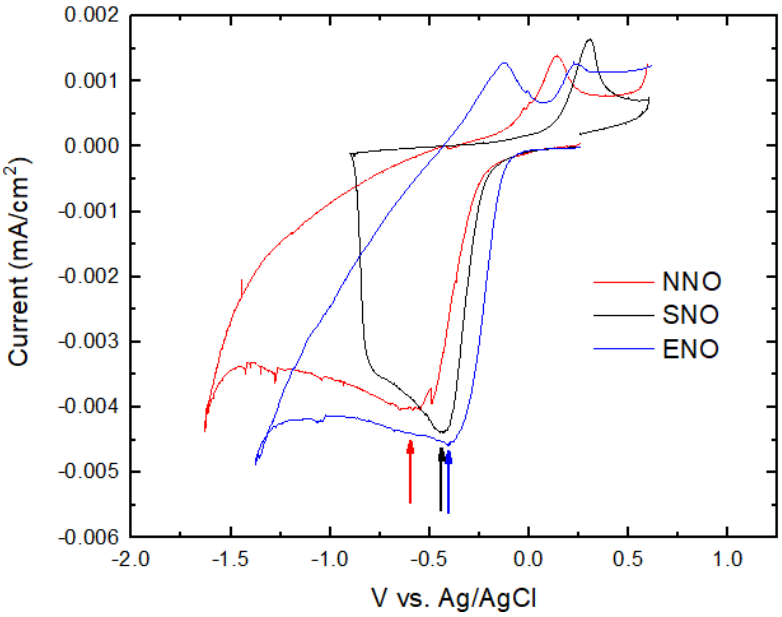

Figure 5-1 Comparison of $RNiO_3$ cyclic voltammograms

Although it is difficult to draw many conclusions from the voltammogram comparison other than the change in maximum current density, this change still makes some intuitive sense. Figure 5-2 shows a comparison of the trend in the $RNiO_3$ series as they undergo this water-mediated phase transition. This figure shows that for the smaller ionic radii [lanthanides with higher atomic mass; $M_w(Eu) > M_w(Sm) > M_w(Nd)$], there is less of a driving force required for the proton intercalation process to occur.

Other trends are difficult to compare because the entire intercalation process may not be complete for the NNO and ENO samples as charge transfer never returns to zero before the ramp in current density near -1.4 V which is attributed to H_2 gas production. Furthermore, it is

important that all samples compared in this matter were prepared in the same batch of annealing because differences in the film structure may affect the voltammograms.

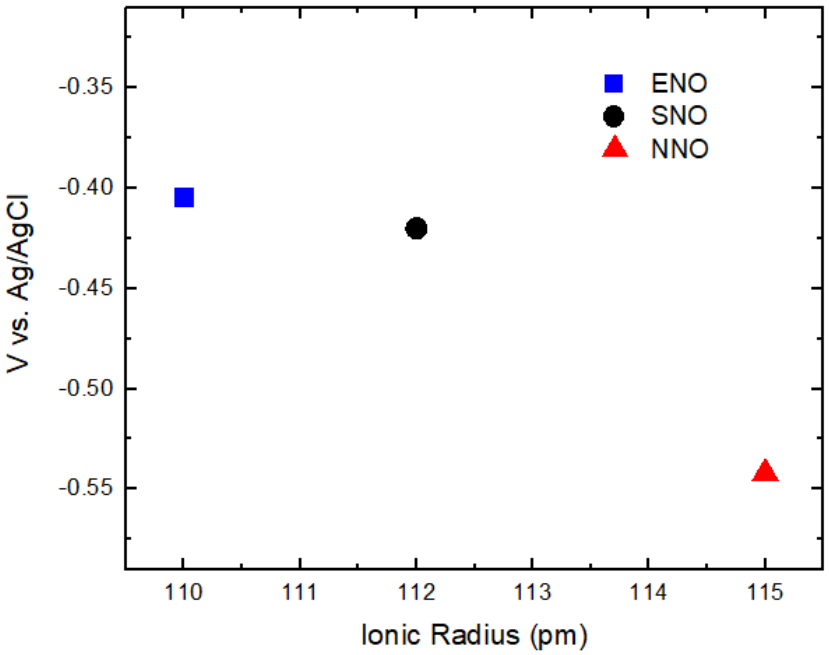

Figure 5-2 Comparison of maximum current density during doping as a fucntion of A-site radius.

5.3 Resistance Switching for $RNiO_3$

Similar to section 5.2, efforts to study the change in the structure – processing connection depended on the preparation $RNiO_3$ thin films of different compositions, subjecting them to similar stimuli and measuring the properties. Figure 5-3 shows the resistance change for ENO, SNO and SNO samples when subjected to bias pulses from 0.1 – 10 s. The change in resistance over this small time period serves to highlight how the parameters of the doping process discussed in chapter 2 generally still affect the $RNiO_3$ compounds, but each in a different way. This set of experiments may also be useful for eventual sensing applications of this new materials phenomena in the nickelates.

The experimental procedure for measuring this switching speed of $RNiO_3$ is slightly different from the other experiments in this study. Specifically, 1 mm channels of ENO, SNO, and NNO were fabricated on LAO substrates by masking off areas with Kapton tape. Annealing was similar to that described in section 5.2. Samples were then treated in a similar fashion to experiments in chapter 2, but the characterization was somewhat different. After doping, Pt paste was applied to the surface of the microchannel in the doped area and allowed to dry before being tested. If the Pt paste were applied to the channel outside the doped area, the resistance was significantly lower (much closer to pristine in all cases). Then after the resistance characterization, the channels were heated at 300 °C for 12 hours to remove all hydrogen and return the film to pristine conditions.

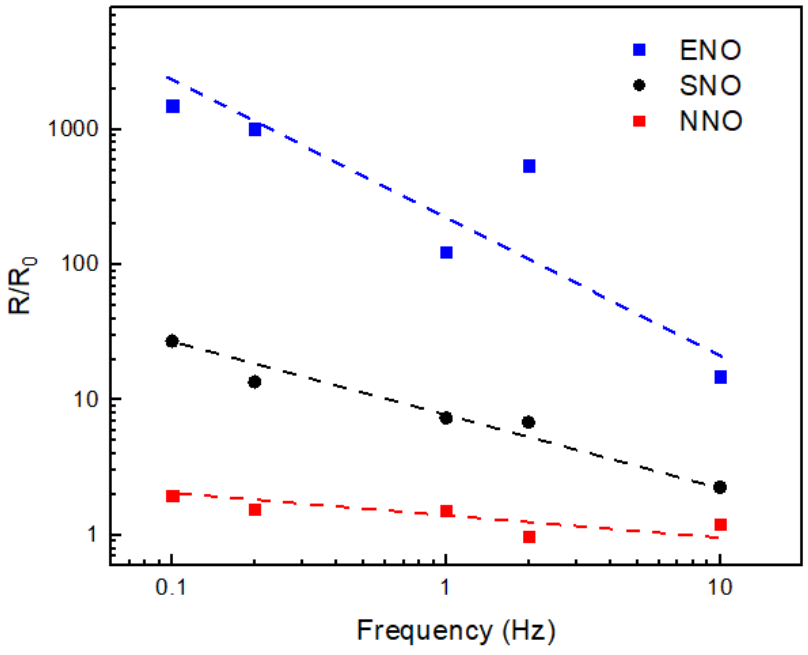

Figure 5-3 Comparison of Resisistance changes for various $RNiO_3$ phase transitions for brief electrostatic pulses.

There are clear trends clear trends in terms of pulse frequency and resistance change for all $RNiO_3$ samples. This is very consistent with previous data showing longer bias applications cause more of a phase change as a larger number of protons are intercalated. The overall trends comparing ENO, SNO, and NNO are shown in Figure 5-4. It can be seen that ENO produces a much greater change in resistance for the all pulse types, specifically the longer ones, whereas NNO barely doubles in resistance. Again, this is very consistent with previous trends across the $RNiO_3$ series discussed here and shown elsewhere showing larger changes for the less stable perovskite structures (in this case ENO) [55].

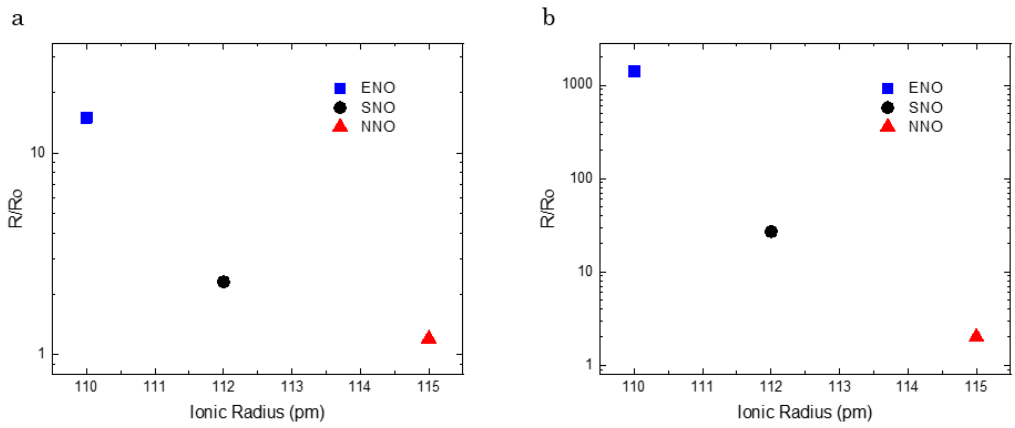

Figure 5-4 Trends for $RNiO_3$ resistance changes as a function of ionic radius for -2.0 V applied for (a) 0.1 s and (b) 10 s.

6. CONCLUSIONS AND FUTURE WORK

6.1 Summary of RNO_3 Characterization

$RNiO_3$ perovskites are crystals with unique metal-insulator phase transitions. Furthermore, trends across the series allow for the tailoring of $RNiO_3$ thin films to be used and tailored for their specific properties. In this work, a new phase transition using charge doping and proton intercalation has been examined. The resulting massive change in resistivity has provided the foundation for more work to be done to help answer the question of why this phenomena occurs. Specifically, characterization of these materials by resistance modulation, voltammetry, XRD, XRR, and NR has been used to study the interrelation between how the processing affects the thin film structure and properties. Ultimately, the understanding between the relationships across structure, process, and properties has provided useful information about trends in the $RNiO_3$ series with which to better leverage thin films and optimize materials performance for devices in the future.

6.2 Implications of Water-Mediated Phase Transition

A major utility of this work is that this unique phase transition in $RNiO_3$ thin films allows for a new modality in sensing. Many different materials respond to changes in applied potential by intercalating ions. However, none of those materials change resistivity to degree that SNO does. When a bias is applied to this unique material it does not just intercalate the protons, it intercalates protons in response to the field in a highly sensitive and detectable manner. Thus it is an essential building block for future research.

One potential application and motivation for some of this research is highlighted in Figure 6-1. Certain aquatic species possess organs which are able to detect electric fields in an aqueous environments. Figure 6-1 highlights how the behavior of a SNO device may mimic this behavior. Specifically, the organ of sharks called the Ampullae of Lorenzini allows for detection of weak electric fields. They use this organ to hunt because fish produce electric fields with their biological processes (e.g. breathing), and it allows the sharks to stalk them effectively at close range. This organ operates as an electric field sensor by moving ions across a membrane in a way that is detectable to the shark's brain. In a similar way, SNO can detectably move ions into its lattice. As such, it may be worth exploring $RNiO_3$ materials in conjunction with some type of aquatic sensing or navigation systems in a way that is not dissimilar from how sharks detect their prey and navigate using this organ [56]. In Figure 6-1, results similar to those of section 5-3 are shown, which show how the resistance changes for positive and negative bias applications (Figure 6-1a). It is also shown what type of marine objects and life create such potentials that may be useful for detection by properly created devices using this new material phenomena technology (Figure 6-1b).

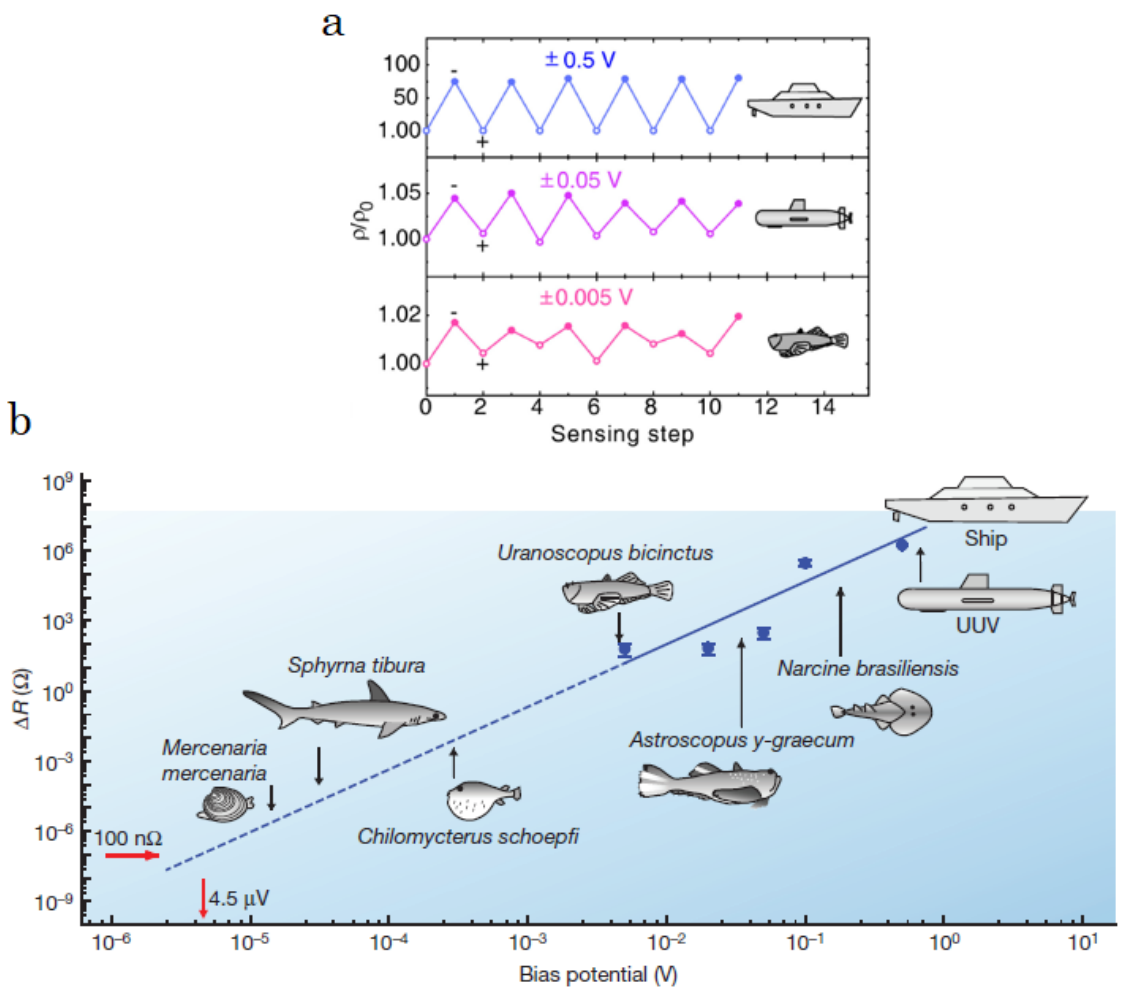

Figure 6-1 Potential electric field sensing application for $RNiO_3$ (a) resistance modulation for applied stimuli and (b) the electric field produced by various aquatic animals and vehicles that may be detected by such fields. The dotted line is extrapolation towards the limits of detectability with high precision equipment [57]–[62] Figure adapted from [5].

6.3 Avenues for Future Studies of $RNiO_3$ doping

There are many exciting areas of research that can be pursued from the basis laid in this work. Including from the application side of aquatic sensing briefly described in the previous section, device fabrication and incorporation of this water-mediated phase change into new

technologies is an obvious avenue of future research. With the large switching in resistance, $RNiO_3$ thin films are ideal for use in sensing devices that require high sensitivity to external stimulus because it has been shown that they provide large detectable changes to small stimuli.

Other, less applied work studying these materials may look further into the effects of this phase transition in $RNiO_3$ and additionally characterize the massive resistance change similar to some of the studies here. Namely, this study has shown that ENO and possibly other $RNiO_3$ with smaller A-site ions may possess even more massive property modulation when encountering electric fields in a water environment. The intercalation of other ions with regards to applied fields may also be studied. Finally, the processing parameters explored here are by no means complete, and there is much room for examination of high salt concentrations or even different solution types and ionic liquid gating. In summary, the future of this line of research should seek to not only better understand why the phase transition occurs and ways to manipulate it, but also to utilize the findings in real world device

APPENDIX. NEUTRON REFLECTOMETRY FITTING

Fitting of the Neutron Reflectivity data was an essential to as a second order data analysis tool after qualitative analysis from the raw data. The NIST Refl1D package [54] is used to build a thin film stack. This software uses 1-dimensional reflectometry to model the density of the thin film as a function of depth. It is based on the curve fitting software Bumps [63]and scattering lengths calculated from PeriodicTable [64]. Python code was written to build up a SNO thin film in these experiments. Tutorials and explanations for how to use the package can be found at [54]. This chapter will briefly discuss the python code used in conjunction with the Refl1D software package.

Constraints are then made upon the different parameters and different algorithms are used to move around in parameter space and reduce the difference between the raw data and the simulated stack. From this analysis method, real and imaginary neutron scattering length density of the film layers, layer thicknesses, and layer surface roughness are able to be extracted with good fits. However, it is absolutely critical to have sufficient information about the film beforehand because there are multiple solutions for each data set. If incorrect information is used or the constraints are not tight enough, an inaccurate fit may be reached. The following is an example fit for one of the samples shown in Figure 4-5 and 4-6. A several layer stack was built to allow some freedom in the model. The following table summarizes the constraints placed upon the different layers. Imaginary SLD was estimated based on the Periodic Table software and not fitted.

Thin Film stack: $Si/SiO_2/SmNiO_3/HSmNiO_3$/Surface layer

0.1 Variable ranges for the Neutron Simulation

Layer	**Neutron SLD (real)**	**Thickness**	**Interface**
Si	3.0-7.0	N/A	0 – 3.5 nm
SiO_2	3.0-7.0	0.2 – 30 nm	0 - 0.55* thickness
$SmNiO_3$	3.0-7.0	0 – 60 nm	0 - 0.55* thickness
$HSmNiO_3$	3.0-7.0	0 – 60 nm	0 - 0.55* thickness
Surface Layer	3.0-7.0	1 – 20 nm	0 - 0.55* thickness

The interface values were computed based on the thickness of the layer because if the surface roughness becomes too large relative to the thickness, the Nevot – Croce approximation is not value. This approximation allows the calculation to run significantly faster.

The program was done with 300k burn in steps and a sample size of 30k with the DREAM algorithm. The results are shown in Figure A-1. The model readout gives a value of X^2 = 2.31, which means there is good agreement between the simulated data and the collected neutron data.

a

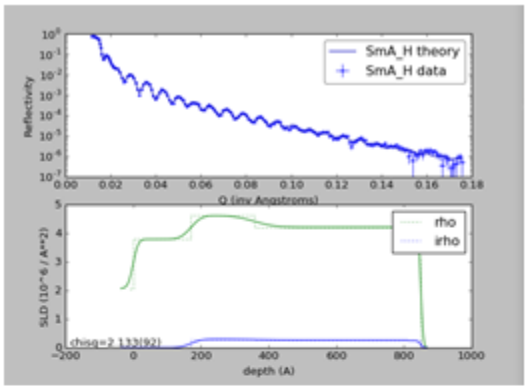

b

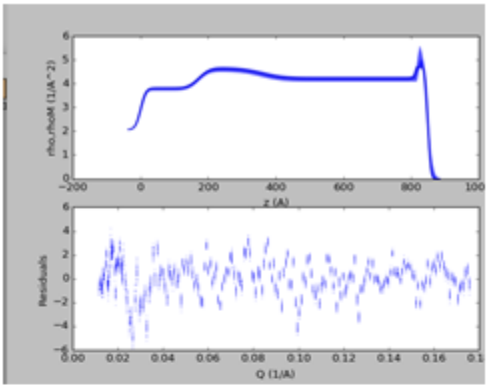

c

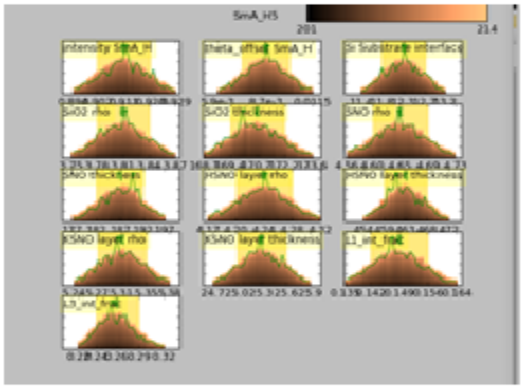

d

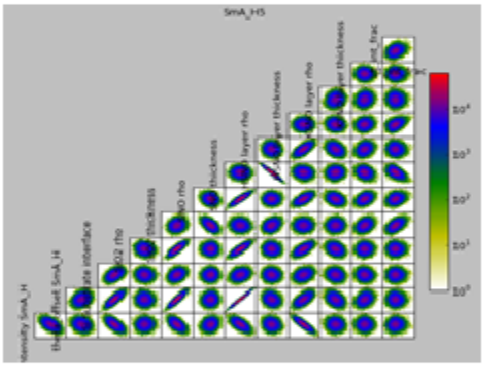

e

[chisq=2.133(92), nllf=197.338]

	Parameter	mean	median	best	68% interval	95% interval
1	intensity SmA_H	0.9094(91)	0.9093	0.9158	[0.900 0.919]	[0.892 0.928]
2	theta_offset SmA_H	8.0(17)e-3	0.00817	0.00805	[0.0064 0.0097]	[0.0042 0.0111]
3	Si Substrate interface	12.20(47)	12.196	12.183	[11.73 12.67]	[11.27 13.10]
4	SiO2 rho	3.801(34)	3.801	3.799	[3.77 3.83]	[3.73 3.87]
5	SiO2 thickness	170.9(15)	170.911	171.089	[169.39 172.34]	[168.09 173.88]
6	SNO rho	4.629(47)	4.630	4.631	[4.58 4.68]	[4.53 4.72]
7	SNO thickness	187.4(50)	187.28	187.00	[182.6 192.5]	[177.5 197.2]
8	HSNO layer rho	4.225(45)	4.228	4.222	[4.18 4.27]	[4.13 4.31]
9	HSNO layer thickness	461.6(73)	462.16	453.24	[453.9 469.0]	[447.3 474.7]
10	KSNO layer rho	5.37(54)	5.308	4.694	[4.75 6.02]	[4.67 6.30]
11	KSNO layer thickness	26.9(70)	24.87	37.52	[19.5 36.1]	[16.6 38.4]
12	L1_int_frac	0.1487(73)	0.1485	0.1460	[0.141 0.156]	[0.135 0.164]
13	L3_int_frac	0.266(25)	0.265	0.259	[0.24 0.29]	[0.22 0.32]
14	L4_int_frac	0.0162(86)	0.0174	0.0040	[0.006 0.025]	[0.001 0.030]
15	L5_int_frac	0.36(15)	0.350	0.171	[0.19 0.53]	[0.16 0.59]

Figure 0-1 Readouts from Refl1d fitting software (a) the SLD profile and overlay with the data. (b) sld profile and variance in comparison to the data. (c) histograms of the frequency of variables taking certain values (d) association between different parameters in the model and (e) summary of data.

REFERENCES

[1] M. A. Green, A. Ho-baillie, and H. J. Snaith, "The emergence of perovskite solar cells," *Nat. Photonics*, vol. 8, no. July, pp. 506–514, 2014.

[2] N. E. Massa, A. Y. Ramos, C. Helio, and L. Medarde, "Structural , magnetic and electronic properties of perovskites (R = rare earth) perovskites (R = rare earth)," *J. Phys. Condens. Matter*, vol. 9, pp. 1679–1707, 1997.

[3] A. M. Glazer, "Simple Ways of Determining Perovskite Structure," *Acta Crystallogr.*, vol. A31, p. 756, 1975.

[4] R. H. Mitchell, *Perovskites Modern and Ancient*. Thunder Bay, Ontario: Almaz Publishing, 2002.

[5] Z. Zhang, D. Schwanz, B. Narayanan, M. Kotiuga, J. A. Dura, M. Cherukara, H. Zhou, J. W. Freeland, J. Li, R. Sutarto, F. He, C. Wu, J. Zhu, Y. Sun, K. Ramadoss, S. S. Nonnenmann, N. Yu, R. Comin, K. M. Rabe, S. K. R. S. Sankaranarayanan, and S. Ramanathan, "Perovskite nickelates as electric-field sensors in salt water," *Nature*, vol. 553, no. 7686, pp. 68–72, 2018.

[6] G. Catalan, "Progress in perovskite nickelate research," *Phase Transitions*, vol. 81, no. 7–8, pp. 729–749, 2008.

[7] S. Catalano, M. Gibert, J. Fowlie, J. Íñiguez, J.-M. Triscone, and J. Kreisel, "Rare-earth nickelates R NiO 3 : thin films and heterostructures," *Reports Prog. Phys.*, vol. 81, no. 4, p. 46501, 2018.

[8] J. A. Alonso, M. J. Martínez-Lope, M. T. Casais, M. A. G. Aranda, and M. T. Fernández-Díaz, "Metal-insulator transitions, structural and microstructural evolution of RNiO3 (R = Sm, Eu, Gd, Dy, Ho, Y) perovskites: Evidence for room-temperature charge disproportionation in monoclinic HoNiO3 and YNiO3," *J. Am. Chem. Soc.*, vol. 121, no. 20, pp. 4754–4762, 1999.

[9] J. L. García-Muñoz, J. Rodríguez-Carvajal, P. Lacorre, and J. B. Torrance, "Neutron-diffraction study of RNiO3 (R=La,Pr,Nd,Sm): Electronically induced structural changes across the metal-insulator transition," *Phys. Rev. B*, vol. 46, no. 8, pp. 4414–4425, 1992.

[10] D. I. Khomskii, *Transition Metal COmpounds*. Cambridge University Press, 2014.

[11] J. Shi, Y. Zhou, and S. Ramanathan, “Colossal resistance switching and band gap modulation in a perovskite nickelate by electron doping,” *Nat. Commun.*, vol. 5, pp. 1–9, 2014.

[12] S. Johnston, A. Mukherjee, I. Elfimov, M. Berciu, and G. A. Sawatzky, “Charge disproportionation without charge transfer in the rare-earth-element nickelates as a possible mechanism for the metal-insulator transition,” *Phys. Rev. Lett.*, vol. 112, no. 10, pp. 1–5, 2014.

[13] Y. Cao, B. Lin, Y. Sun, H. Yang, and X. Zhang, “Sr-doped lanthanum nickelate nanofibers for high energy density supercapacitors,” *Electrochim. Acta*, vol. 174, no. 1, pp. 41–50, 2015.

[14] D. K. Hwang, S. Kim, J.-H. Lee, I.-S. Hwang, and I.-D. Kim, “Phase evolution of perovskite LaNiO 3 nanofibers for supercapacitor application and p-type gas sensing properties of LaOCl–NiO composite nanofibers,” *J. Mater. Chem.*, vol. 21, no. 6, pp. 1959–1965, 2011.

[15] L. Chang, L. Wang, L. You, Y. Zhou, L. Fang, S. Wang, and J. Wang, “Band gap tuning of nickelates for photovoltaic applications,” *J. Phys. D. Appl. Phys.*, vol. 49, no. 44, 2016.

[16] T. Ling, Z. Chen, and M. Lee, “for oxidation of C2HsOH , CH3CHO , and CH4,” vol. 26, pp. 79–86, 1995.

[17] L. Xuchen, “Preparation and characterization of LaNiO 3 A r F ratio-sensitive thin film by sol – gel process based on amorphous citrate precursors,” pp. 24–28, 2000.

[18] Y. Zhou, X. Guan, H. Zhou, K. Ramadoss, S. Adam, H. Liu, S. Lee, J. Shi, M. Tsuchiya, D. D. Fong, and S. Ramanathan, “Strongly correlated perovskite fuel cells,” *Nature*, vol. 534, no. 7606, pp. 231–234, 2016.

[19] Z. Li, Y. Zhou, H. Qi, Q. Pan, Z. Zhang, N. N. Shi, M. Lu, A. Stein, C. Y. Li, S. Ramanathan, and N. Yu, “Correlated Perovskites as a New Platform for Super-Broadband-Tunable Photonics,” *Adv. Mater.*, vol. 28, no. 41, pp. 9117–9125, 2016.

[20] S. D. Ha, J. Shi, Y. Meroz, L. Mahadevan, and S. Ramanathan, “Neuromimetic circuits with synaptic devices based on strongly correlated electron systems,” *Phys. Rev. Appl.*, vol. 2, no. 6, pp. 1–11, 2014.

[21] S. Hyeon Lee, M. Kim, S. D. Ha, J. W. Lee, S. Ramanathan, and S. Tiwari, “Space charge polarization induced memory in SmNiO3/Si transistors,” *Appl. Phys. Lett.*, vol. 102, no. 7, 2013.

[22] G. J. M. Janseen and W. C. Nieuwpoort, “Band gap in NiO: A cluster study,” *Phys. Rev. B*, vol. 38, no. 5, pp. 3449–3458, 1988.

[23] F. Zuo, P. Panda, M. Kotiuga, J. Li, M. Kang, C. Mazzoli, H. Zhou, A. Barbour, S. Wilkins, B. Narayanan, M. Cherukara, Z. Zhang, S. K. R. S. Sankaranarayanan, R. Comin, K. M. Rabe, K. Roy, and S. Ramanathan, “Habituation based synaptic plasticity and organismic learning in a quantum perovskite,” *Nat. Commun.*, vol. 8, no. 1, pp. 1–7, 2017.

[24] R. Jaramillo, F. Schoofs, S. D. Ha, and S. Ramanathan, “High pressure synthesis of SmNiO3 thin films and implications for thermodynamics of the nickelates,” *J. Mater. Chem. C*, vol. 1, no. 13, p. 2455, 2013.

[25] S. D. Ha, R. Jaramillo, D. M. Silevitch, F. Schoofs, K. Kerman, J. D. Baniecki, and S. Ramanathan, “Hall effect measurements on epitaxial SmNiO3 thin films and implications for antiferromagnetism,” *Phys. Rev. B - Condens. Matter Mater. Phys.*, vol. 87, no. 12, pp. 1–9, 2013.

[26] S. D. Ha, M. Otaki, R. Jaramillo, A. Podpirka, and S. Ramanathan, “Stable metal-insulator transition in epitaxial SmNiO 3 thin films,” *J. Solid State Chem.*, vol. 190, pp. 233–237, 2012.

[27] G. H. Aydogdu, S. D. Ha, B. Viswanath, and S. Ramanathan, “Epitaxy, strain, and composition effects on metal-insulator transition characteristics of SmNiO3 thin films,” *J. Appl. Phys.*, vol. 109, no. 12, 2011.

[28] B. Torriss, J. Margot, and M. Chaker, “Metal-Insulator Transition of strained SmNiO3 Thin Films: Structural, Electrical and Optical Properties,” *Sci. Rep.*, vol. 7, no. October 2016, p. 40915, 2017.

[29] Q. Liu, G. Zhao, G. Zhao, and L. Lei, “Fabrication of LaNiO 3 Thin Film on the Si-Substrate by Sol-Gel Process,” vol. 695, pp. 585–588, 2011.

[30] M. Akiyama, J. Tamaki, N. Miura, and N. Yamazoe, “Tungsten Oxide-Based Semiconductor Sensor Highly Sensitive to NO and NO2.,” *Chemistry Letters*. pp. 1611–1614, 1991.

[31] S. R. Morrison, “Semiconductor gas sensors,” *Sensors and Actuators*, vol. 2, pp. 329–341, 1982.

[32] S. J. Ippolito, S. Kandasamy, K. Kalantar-Zadeh, and W. Wlodarski, “Hydrogen sensing characteristics of WO3thin film conductometric sensors activated by Pt and Au catalysts,” *Sensors Actuators, B Chem.*, vol. 108, no. 1–2 SPEC. ISS., pp. 154–158, 2005.

[33] N. Yamazoe, G. Sakai, and K. Shimanoe, “Oxide semiconductor gas sensors,” *Catal. Surv. from Asia*, vol. 7, no. 1, pp. 63–75, 2003.

[34] J. B. Goodenough, “Metallic oxides,” *Prog. Solid State Chem.*, vol. 5, no. C, pp. 145–399, 1971.

[35] G. A. Niklasson and C. G. Granqvist, “Electrochromics for smart windows: Thin films of tungsten oxide and nickel oxide, and devices based on these,” *J. Mater. Chem.*, vol. 17, no. 2, pp. 127–156, 2007.

[36] M. Hübner, C. E. Simion, A. Haensch, N. Barsan, and U. Weimar, “CO sensing mechanism with WO3based gas sensors,” *Sensors Actuators, B Chem.*, vol. 151, no. 1, pp. 103–106, 2010.

[37] C. G. Granqvist, “Electrochromic tungsten oxide films: Review of progress 1993-1998,” *Sol. Energy Mater. Sol. Cells*, vol. 60, no. 3, pp. 201–262, 2000.

[38] R. J. Mortimer, “Electrochromic Materials,” *Chem. Soc. Rev.*, vol. 26, pp. 147–156, 1997.

[39] T. Oi, “Electrochromic materials A,” *Annu. Rev. Mater. Sci.*, 1986.

[40] C. G. Granqvist, “Progress in electrochromics: tungsten oxide revisited,” *Electrochim. Acta*, vol. 44, no. 18, pp. 3005–3015, 1999.

[41] S. Thakoor, A. Moopenn, T. Daud, and A. P. Thakoor, “Solid-state thin-film memistor for electronic neural networks,” *J. Appl. Phys.*, vol. 67, no. 6, pp. 3132–3135, 1990.

[42] P. A. Lee, N. Nagaosa, and X.-G. Wen, “Doping a Mott Insulator: Physics of High Temperature Superconductivity,” *Rev. Mod. Phys.*, pp. 1–69, 2004.

[43] K.-C. Ho, T. G. Rukavina, and C. B. Greenberg, “Tungsten oxide-prussian blue electrochromic system based on a proton-conducting polymer electrolyte,” *J. Electrochem. Soc.*, vol. 141, no. 8, pp. 2061–2067, 1994.

[44] X. Leng, J. Pereiro, J. Strle, G. Dubuis, A. T. Bollinger, A. Gozar, J. Wu, N. Litombe, C. Panagopoulos, D. Pavuna, and I. Božović, “Insulator to metal transition in WO3 induced by electrolyte gating,” *npj Quantum Mater.*, vol. 2, no. 1, p. 35, 2017.

[45] S. Nishihaya, M. Uchida, Y. Kozuka, Y. Iwasa, M. Kawasaki, S. Nishihaya, M. Uchida, Y. Kozuka, Y. Iwasa, M. Kawasaki, Y. Iwasa, and M. Kawasaki, "Evolution of Insulator-Metal Phase Transitions in Epitaxial Tungsten Oxide Films during Electrolyte-Gating," *ACS Appl. Mater. Interfaces*, vol. 8, no. 34, pp. 22330–22336, 2016.

[46] P. Kritzer, "Corrosion in high-temperature and supercritical water and aqueous solutions: A review," *J. Supercrit. Fluids*, vol. 29, no. 1–2, pp. 1–29, 2004.

[47] A. J. Bard, L. R. Faulkner, J. Leddy, and C. G. Zoski, *Electrochemical Methods: Fundamentals and APplications*, 1st, Vol. ed. Wiley, 1980.

[48] R. G. Compton and C. E. Banks, *Understanding Voltammetry*, 1st ed. World Scientific Publishcing Co. Pte. Ltd., 2007.

[49] N. Elgrishi, K. J. Rountree, B. D. McCarthy, E. S. Rountree, T. T. Eisenhart, and J. L. Dempsey, "A Practical Beginner's Guide to Cyclic Voltammetry," *J. Chem. Educ.*, vol. 95, no. 2, pp. 197–206, 2018.

[50] "Linear Sweep and Cyclic Voltametry: The Principles." [Online]. Available: https://www.ceb.cam.ac.uk/research/groups/rg-eme/teaching-notes/linear-sweep-and-cyclic-voltametry-the-principles.

[51] R. Guidelli, R. G. Compton, J. M. Feliu, E. Gileadi, J. Lipkowski, W. Schmickler, and S. Trasatti, "Defining the transfer coefficient in electrochemistry: An assessment (IUPAC Technical Report)," *Pure Appl. Chem.*, vol. 86, no. 2, pp. 245–258, 2014.

[52] "Neutron scattering lengths and cross sections." [Online]. Available: https://www.nist.gov/ncnr/planning-your-experiment/sld-periodic-table.

[53] D. Pelloquin, N. Barrier, A. Maignan, and V. Caignaert, "Reactivity in air of the Sr3Co2O7-δRP = 2 phase: Formation of the hydrated Sr3Co2O5(OH)2ṡxH2O cobaltite," *Solid State Sci.*, vol. 7, no. 7, pp. 853–860, 2005.

[54] B. Kirby, "NCNR Reflectometry Software." [Online]. Available: https://www.ncnr.nist.gov/reflpak/.

[55] J. Chen, Y. Zhou, S. Middey, J. Jiang, N. Chen, L. Chen, X. Shi, M. Döbeli, J. Shi, J. Chakhalian, and S. Ramanathan, "Self-limited kinetics of electron doping in correlated oxides," *Appl. Phys. Lett.*, vol. 107, no. 3, 2015.

[56] A. J. Kalmijn, "The Electric and Magnetic Sense of Sharks, Skates, and Rays," pp. 45–52, 1974.

[57] C. N. Bedore and S. M. Kajiura, “Bioelectric Fields of Marine Organisms: Voltage and Frequency Contributions to Detectability by Electroreceptive Predators,” *Physiol. Biochem. Zool.*, vol. 86, no. 3, pp. 298–311, 2013.

[58] V. D. Baron, “Electric discharges of two species of stargazers from the South China Sea (Uranoscopidae, Perciformes),” *J. Ichthyol.*, vol. 49, no. 11, pp. 1065–1072, 2009.

[59] M. Hirota, “a Method To Measure Ship ’ S Underwater Electric Field From Deck,” pp. 224–228.

[60] J. G. Kim, J. H. Joo, and S. J. Koo, “Development of high-driving potential and high-efficiency Mg-based sacrificial anodes for cathodic protection,” *J. Mater. Sci. Lett.*, vol. 19, no. 6, pp. 477–479, 2000.

[61] M. V Bennett, M. Wurzel, and H. Grundfest, “The Electrophysiology of Electric Organs of Marine Electric Fishes : I. Properties of electroplaques of Torpedo nobiliana.,” *J. Gen. Physiol.*, vol. 44, no. 4, pp. 757–804, 1961.

[62] R. Mathewson, A. Mauro, E. Amatniek, and H. Grundfest, “Morphology of Main and Accessory Electric Organs of Narcine brasiliensis (Olfers) and Some Correlations with Their Electrophysiological Properties,” *Univ. Chicago Press Journals*, vol. 115, no. 1, pp. 126–135, 2018.

[63] P. Kienzle, “Bumps : Curve Fitting and Uncertainty Analysis,” 2013.

[64] “Extensible Periodic Table.” [Online]. Available: http://periodictable.readthedocs.io/en/latest/index.html.